

1
2
3
4
5
6
7
8
9
10
11
12
13
14
15
16
17
18
19
20

This manuscript is a preprint and has been formally accepted for publication in **Tectonics**.

Salt-detached strike-slip faulting, Outer Kwanza Basin, Offshore Angola

Aurio Erdi^{1,2}, Christopher A-L. Jackson^{1, †}

¹Basin Research Group (BRG), Department of Earth Science and Engineering, Imperial College, Prince Consort Road, London, SW7 2BP, UK

²National Research and Innovation Agency (BRIN), Indonesia

[†]Present address: Jacobs, 5 First Street, Manchester, Greater Manchester, M15 4GU, UK

Corresponding author: Aurio Erdi (a.erd18@imperial.ac.uk)

Key Points:

- Strike-slip faults grew in the Outer Kwanza Basin to accommodate along margin variations in the rate and magnitude of salt-detached overburden translation
- The faults nucleated as isolated segments during the Early Cretaceous, propagating and linking during the subsequent c. 77 Myr
- Displacement-distance scaling relationships display significant scatter, likely reflecting kinematic interactions between faults within the array

21 **Abstract**

22 We here use a 3D seismic reflection dataset from the Outer Kwanza Basin, offshore Angola
23 to examine the structure and growth of salt-detached strike-slip faults. The faults occur in four, up
24 to 13.8 km-long, NE-trending arrays that are physically linked by restraining bends and releasing
25 stepovers, and which presently overlie Aptian salt and base-salt relief related to pre-salt faulting.
26 We suggest that these faults formed to accommodate along-margin variations in the rate and
27 magnitude of differential seaward translation and salt diapirism, which commenced in the Early
28 Cretaceous. We illustrate that the arrays grew by tip propagation of isolated fault segments, some
29 of which linked during the Albian-Cenomanian (i.e., 113-100.5 Ma, or the initial 11-13% of their
30 deformation history). Some arrays then reached their near-final length within the subsequent ca.
31 77 Ma, or the next 69-81% of their deformation history), while others attained this later, during
32 the subsequent ca. 18 Ma (i.e., after 95% of their deformation history). During this time, the
33 segments formed and then breached releasing and restraining stepovers, with the arrays as a whole
34 growing by alternating periods of lengthening and, throw accumulation, punctuated by phases of
35 inactivity. Our results also show that scatter in the D-L scaling of strike-slip faults reflect the
36 propagation, interaction, and linkage of individual segments.

37 **Plain Language Summary**

38 Strike-slip faulting is a key way in which the Earth's crust deforms, occurring when two slabs
39 of rock or sediment slide past each other. Strike-slip faults can be very big, defining the margins
40 of the Earth's tectonic plates, or can be relatively small, forming at the edges of landslides. Despite
41 being widespread, the lack of natural geological examples exposed at the Earth's surface or imaged
42 within the Earth means we have a poor understanding of the three-dimensional shape of strike-slip
43 faults or how they grow over millions of years. In this study we use (seismic reflection) images of
44 the rocks below the seabed offshore Angola, West Africa to reveal the geometry and deformation
45 history of relatively large (i.e., kilometre-scale) strike-slip faults formed due to the sliding of
46 sediments on salt, a rock weak enough to behave like a fluid over millions of years. It is likely
47 these faults formed because sediments slid towards the Atlantic Ocean by differencing amounts.
48 We show that these faults form due to the lateral and vertical linkage of smaller faults over several
49 tens of millions of years.

50 **1. Introduction**

51 Strike-slip faults are a prominent mode of crustal deformation, typically forming to
52 accommodate differential movement between horizontally translating rock masses (Bates and
53 Jackson, 1997; Christie-Blick and Biddle, 1985; Sylvester, 1988). Strike-slip faults are widespread
54 on Earth, occurring in a range of settings and being of widely varying scales (Mann, 2007). For
55 example, very large thick-skinned (i.e. basement-involved) strike-slip faults can form at and define
56 plate boundaries (Sylvester, 1988; Cunningham and Mann, 2007), whereas relatively small, thin-
57 skinned (i.e. basement-decoupled) strike-slip faults can define the margins of submarine landslides
58 (e.g. Bull et al., 2009), or blocks of material sliding on shale- (e.g. Escalona and Mann, 2006;
59 Leduc et al, 2012) or salt-rich (e.g. Cartwright et al, 2012; Fernandez et al, 2020) detachments
60 (Fig. 1a-d). In all of these settings, the faults are characterized by complex alternations between
61 reverse- and normal-throws, with geometrically or kinematically defined segments marked by
62 relatively sharp changes in fault strike that define restraining or releasing bends or stepovers (e.g.
63 Christie-Blick and Biddle, 1985; Cunningham and Mann, 2007). Although numerous studies have
64 focused on the geometry and kinematics of strike-slip faults arrays, most are limited in that they:
65 (a) only provide a two- (i.e. in map and/or profile view) rather than three-dimensional assessment;
66 and/or (b) do not integrate growth strata and analysis of piercing points to determine fault
67 kinematics. Exceptions to this are the field-based studies of Peacock (1991), Kim et al. (2000 and
68 2001), Nixon et al (2011) and Nicol et al. (2017), and the 3D-seismic reflection data-based studies
69 of Benesh et al. (2014), Omosanya et al. (2017), and Deng et al. (2019). Thus, in stark contrast to
70 normal (e.g. Walsh and Watterson, 1988; Dawers et al., 1993; Cartwright et al., 1995; Walsh et
71 al., 2002; Childs et al., 2017; Rotevatn et al., 2019) and even reverse (e.g. Higgins et al., 2009;
72 Bergen and Shaw, 2010) faults, which have been extensively studied, we have a relatively poor
73 understanding of the four-dimensional structure and growth of strike-slip fault arrays.

74 Salt basins represents an ideal location in which to study strike-slip fault arrays. In these
75 locations, thin-skinned (i.e. salt-detached) strike-slip faults may form in the salt overburden to
76 accommodate: (1) regional variability in the rate and direction of salt and overburden flow (e.g.
77 Rowan et al, 1999; Fort and Brun, 2012) (Fig. 1a, c); and/or (2) local differential extensional or
78 contractional strains in the overburden (Fig. 1b) (e.g. Duval et al., 1992; Cartwright et al., 2012).
79 Physical models have specifically shown that spatial changes in salt thickness related to base-salt
80 relief influence this differential flow and resultant strains, and thus control fault segment

81 nucleation, growth, and linkage (Fig. 1e, f) (Dooley and Schreurs, 2012; Dooley et al, 2017).
82 Despite providing an improved understanding of the geometry and kinematics of salt-detached
83 strike-slip fault arrays, which may provide insights into arrays formed or forming in other settings,
84 physical model predictions need testing with observations from natural systems.

85 This study represents a first attempt to document the three-dimensional geometry and
86 kinematics of a salt-detached strike-slip fault array developed on salt-bearing passive margins. To
87 do this we use high-quality 3D seismic reflection data from the Outer Kwanza Basin, offshore
88 Angola. These data allow us to constrain the geometry of constituent fault segments and systems,
89 showing the arrays grew to accommodate the differential seaward translation rate of salt and its
90 overburden, as well as salt diapirism. We also show the faults are variably linked and have
91 boundaries defined by restraining bends and releasing stepovers. We also assess isopach (i.e.
92 thickness) maps and throw patterns, and undertake throw backstripping to reconstruct the evolution
93 of the array. Using these data, we assess the growth trajectory of faults within displacement-
94 distance (D-L) scaling space, highlighting the key roles throw accumulation, lateral propagation
95 and linkage play in controlling fault array development, in a manner similar to that documented
96 for normal and reverse faults.

97

98 **2. Geological Setting**

99 Our study area is located in the Outer Kwanza Basin, a sub-basin of the salt-bearing passive
100 margin of the Kwanza Basin, offshore Angola (e.g. Hudec and Jackson, 2002; 2004) (Fig. 2). The
101 Outer Kwanza Basin stretches between the basement high of the Flamingo Platform in the east and
102 the Angola Abyssal Plain in the west. The basin is bounded to the south by several volcanic
103 seamounts that separate it from Benguela Basin, whereas to the north it passes into the Lower
104 Congo Basin.

105 Rifting of the Kwanza Basin initiated during the Early Cretaceous, associated with the opening
106 of the South Atlantic Ocean. Rifting occurred in response to NE-oriented extension (e.g. Maurin
107 and Guiraud, 1993; Guiraud et al, 2010), which was partly accommodated by the formation of NE-
108 trending transform faults (Fig. 2a) (Guiraud et al., 2010). In the Outer Kwanza Basin, these
109 transform faults bound arrays of rift-related, NW-trending, horst-and-graben structures (Fig. 2b)
110 (Erdi and Jackson, 2021). During the latter stage of rifting, a thick layer (up to 4 km) Aptian salt

111 unit was deposited. This salt layer thickened seaward (i.e. westward) and along-strike (i.e.
112 southward) (von Nicolai, 2011; Evans and Jackson, 2019), draping relief associated with the
113 underlying rift-related structures (Fig. 2b) (e.g. Hudec and Jackson, 2004; Erdi and Jackson, 2021).

114 Since the deposition of Aptian salt, salt tectonics has strongly influenced the tectono-
115 stratigraphic development of the Outer Kwanza Basin, principally through thin-skinned, gravity-
116 driven deformation (e.g. Duval et al., 1992; Lundin, 1992; Marton et al., 2000). The gravity-driven
117 deformation is expressed as kinematically-linked zones of updip extension above the Flamingo
118 Platform, and downdip contractional toward the seaward edge of the salt (Fig. 2a) (Hudec and
119 Jackson, 2004). These two zones are connected by an intermediate zone of translation that has
120 undergone multiple phases of extension and contraction due to salt and overburden flow over
121 prominent base-salt relief (Evans and Jackson, 2019; Erdi and Jackson, 2021). Overall, the
122 overburden has translated seaward up to 23 km (Jackson and Hudec, 2005), with local rotations of
123 up to c. 32° (Evans and Jackson, 2019) and salt-detached strike-slip faulting (i.e. tear fault; Lundin,
124 1992 or transfer fault; Duval et al., 1992) accommodating the variable rate and magnitude of the
125 seaward flux of salt and its overburden. Critically, the horizontal translation of salt and its
126 overburden mean that overburden structures (including the strike-slip fault arrays) are unlikely to
127 be the same position as where they formed, nor do they directly overlie the base-salt features that
128 triggered their initial development (see Erdi and Jackson, 2021).

129 A recent study illustrates that although overburden strike-slip faults have similar strikes and are
130 locally physically-linked with the NE-trending, basement-involved transform fault, they are of
131 different ages and are kinematically separate systems, i.e., the overburden strike-slip faults are
132 post- (rather than pre-) Aptian and formed to accommodate along-strike differences in salt-related
133 contraction and/or extension, (rather than basement-involved, subsalt blocks) (Fig. 2b) (Erdi and
134 Jackson, 2021). In this study, we focus on the three-dimensional geometry and kinematic analysis
135 of four large strike-slip faults within the broader array.

136

137 **3. Dataset and Methods**

138 **3.1. Dataset**

139 We use a post-stack depth-migrated BroadSeis™ 3D seismic reflection dataset that covers c.
140 714 km² of Outer Kwanza Basin, Offshore Angola (Fig. 2a). This dataset images down to the base

141 of the Aptian salt (c. -5.5 km), with an estimated spatial resolution of c. 3.5 ($\lambda=14$ m) at the seabed
142 and c. 30 m ($\lambda=120$ m) at a depth of 5 km. The dataset has a record length of 10 s (although the
143 image is truncated at base-salt), a vertical sampling rate of 2 ms, and a line spacing of 25 m, with
144 inlines and crosslines being oriented normal and perpendicular, respectively, to the broadly
145 southwestward-directed, tectonic transport (i.e. translation) direction. The data are displayed with
146 the SEG ‘reverse’ convention, where a downward increase and a decrease in acoustic impedance
147 are represented by negative (white) and positive (black) reflection events, respectively.

148

149 **3.2 Stratigraphy and structural framework**

150 We map eight seismic horizons (i.e. base-salt, Aptian salt, Albian, Eocene, Oligocene, Lower
151 Miocene, Upper Miocene, and seabed) across the study area using the seismic-stratigraphic
152 framework of Erdi and Jackson (2021). These horizons are used to generate structure maps that
153 allowed us to determine the three-dimensional geometry of the base-salt surface, and overlying
154 salt and overburden structures, including the salt-detached strike-slip fault array (see section 3.3;
155 Fig. 3). We overlay structure maps to show *present* distribution and relationship between base-
156 salt, salt structures, and the strike-slip faults (Fig. 4c) (c.f. Pichel et al., 2019 and Erdi and Jackson,
157 2021). We also generate salt and overburden isopach maps, which reveal the present structure of
158 the salt layer and the timing of overburden deformation, respectively (Fig. 4a, b). Finally, we
159 generate variance maps (e.g. Bahorich and Farmer, 1995) along specific seismic horizons to map
160 faults and piercing points (e.g. channels) (Figs 5 and 6).

161

162 **3.3 Analysis of fault geometry and kinematics**

163 We use the following five techniques to document the three-dimensional geometry and
164 kinematics of salt-detached, strike-slip faults: 1) displacement-distances analysis (Tx) (Fig. 3a-c);
165 2) displacement backstripping (e.g. Petersen et al., 1992; Rowan et al., 1998; Dutton and Trudgill,
166 2009; Jackson et al., 2017); 3) fault growth trajectory plotting (see Rotevatn et al., 2019 and Pan.,
167 et al., 2022); 4) throw-depth analysis (Tz; e.g. Mansfield and Cartwright, 1996; Cartwright et al.,
168 1998; Tvedt et al., 2016; Jackson and Rotevatn, 2013) (Fig. 3d-e); 5) expansion indices analysis
169 (EI) (e.g. Thorsen, 1963; Jackson and Rotevatn, 2013; Reeve et al., 2015; Tvedt et al., 2016) (Fig.
170 3f); and, 6) isopach map analysis (e.g. Jackson and Rotevatn, 2013; Tvedt et al., 2016) (Fig. 7) (see

171 Appendix A for full details of these various methods). Our determination of Tx (i.e., the point of
172 maximum throw on the fault) is defined by constraining their lateral offset and throw. The lateral
173 offset is defined by measuring the *horizontal* offset of piercing points across structures (i.e., salt
174 structures, faults, and channels) (e.g., Peacock, 1991; Kim et al., 2001), whereas the throw is
175 defined by measuring, in two-dimensional cross-sectional view, the *vertical* displacement of
176 stratigraphic horizons (e.g., Omosanya et al., 2017; Deng et al., 2019).

177

178 **4. Structural Framework**

179 **4.1 Base-salt**

180 The stratigraphic surface defining the base of the salt (base-salt) broadly dips to the southwest
181 and is characterized by three distinct trends of relatively steeply dipping ($>10^\circ$) areas called
182 ‘ramps’ (Fig. 4a). The first trend is defined by NW-trending ramps that are up to c. 13 km long
183 and which, in the northeast of the study area, define the southwestward edge of the Flamingo
184 Platform (see Fig 2a). The second trend is represented by N-trending ramps that are up to c. 10 km
185 long, and which occur in the central and south-eastern parts of the study area. Between these first
186 two trends, we observe three sub-triangular, local structural highs, which have relief of up to c. 1
187 km (U, V, W; Fig. 4a). The long axes of these structural highs trend broadly NW-to-N, and they
188 dip either basinward (i.e. to the SW) or landward (i.e. to the NE). The N-trending ramps and
189 associated local structural highs may be relicts of the Angola-Gabon horst-block systems that
190 formed during Early Cretaceous rifting (e.g. Hudec and Jackson, 2004; Erdi and Jackson, 2021).
191 The third set of base-salt ramps trend NE and thus intersect the NW-trending ramps. They are up
192 to c. 6 km long and dip either NW or SE and (Fig. 4a). These ramps are parallel to basement-
193 involved transfer fault zones (e.g., the Martin Vaz Fault Zone in Fig 2a; Moulin et al., 2005;
194 Guiraud et al., 2010) and may thus be the upper crustal expression of these lithosphere-scale
195 structures (Erdi and Jackson, 2021).

196

197 **4.2 Salt structures**

198 The salt isopach map shows that Aptian salt has flowed to form a suite of salt structures (e.g.,
199 anticlines, walls) that are locally separated by apparent primary salt welds (Fig. 4b, c) (*sensu*
200 Wagner and Jackson, 2011). Secondary welds separate minibasins adjacent to squeezed diapirs

201 (SN and SQ; Fig. 9). Salt anticlines (SA and SN) are >0.5 km wide, >1.3 km long, and have vertical
202 relief up to 0.7 km, whereas salt walls (SW and SQ) are far larger, being >1.1 km wide, up to 47
203 km long, and having vertical relief of up to 3 km (Fig. 9), extending from the Aptian source layer
204 up to the seabed (i.e. SW2; Erdi and Jackson, 2021).

205

206 **4.3 Supra-salt structural styles**

207 The distribution and style of supra-salt structures vary across the study area and are best-
208 illustrated with variance attribute maps (Fig. 5). These maps show that normal, thrust, and salt-
209 detached strike-slip faults are common, with these structures being at least c. 2 km, 5 km, and 5
210 km long, respectively. These faults have variable trends and spatial relationships, lying parallel,
211 perpendicular, or oblique to one another and adjacent salt structures (Fig. 5). Erdi and Jackson
212 (2021) explore the geometry and timing of growth of the various salt structures and related normal
213 and thrust faults, and how these relate to the geometry of the base salt surface. We here focus on
214 the strike-slip fault array.

215

216 **5. Geometry of Salt-detached Strike-slip Faults**

217 **5.1 Overall structure**

218 We observe five, NE-to-NNE-striking, salt-detached strike-slip fault systems that show
219 increasingly complex geometries upwards within the cover strata (F1-5; Figs 4b and 5). They are
220 broadly characterised by a long (up to 13 km), approximately linear fault traces, that terminate
221 against normal faults, die-out into salt structures, or simply terminate upwards within the
222 overburden. The trace length of F4 (i.e. F4a, b) increases upwards, but decreases upward for F1-
223 F3. At the top Albian, F3-F4a have long, linear fault traces (Figs 5a and 6b), whereas F1-F2
224 comprise a main structure (F1a and F2a) and an antithetic array (F1b and F2b) that are physically-
225 linked; in these latter cases, these zones of linkage are defined by asymmetrical, graben-like
226 structural lows (i.e. negative flower structures; e.g. Harding, 1985; Sylvester, 1988; Leduc et al.,
227 2012), reflecting extensional stepover (Figs 5a, 6a, 10b-f). Shallower in the stratigraphy, at the
228 top Eocene, although the long, linear fault traces still exist, many faults are characterized by several
229 short (up to 5 km long) segments, giving rise to an overall *en echelon* pattern. Individual segments
230 are hard- or soft-linked (F1-F4a; Figs 5b) (sensu Peacock & Sanderson, 1994; 1995). For example,

231 segments defining F3 are physically linked, whereas those associated with F2 are physically
232 unlinked and separated by a relay zone (Fig. 6c-d). At this structural level, we also observe normal
233 fault-dominated splay zone between F1 and the F2 and at the northeastern lateral tip of F4a (Figs
234 5b and 6c-d). Only F1a and F4a and F4b and their antithetic array (F1b and F4c) extend up to the
235 structural level of the top Miocene, where they are defined by relatively continuous traces and
236 separated by an extensional stepover (Figs 5c and 6e-f).

237 In addition to displaying vertical changes in map-view geometry, salt-detached strike-slip faults
238 vary in terms of their cross-sectional geometry and vertical extent (Fig. 10). The faults are
239 moderate-to-steep dipping (45° - 80°) and are generally characterized by normal and/or reverse
240 throws of up to 830 m. In cross-section, it is also clear that the faults increase in height seaward,
241 dying-out upward into progressive younger stratigraphy. For example, in the NE they tip-out into
242 intra-Oligocene strata, whereas in the SW they tip-out into Miocene strata or extend to the present
243 seabed (Figs 5-6 and cf. Fig. 10a-e and f-g).

244 We observe many unequivocal piercing points along strike of the strike-slip faults and at various
245 structural levels (e.g. salt anticlines and walls, normal and thrust faults, and channels). These points
246 define sinistral lateral offsets of up to 1.6 km (Figs 4-6). First, at the top salt, the faults offset
247 presumably older (i.e. pre-existing) salt structures (SQ1, SQ2a-b, SN1a-b, SA2-5; Fig. 4b).
248 Second, at shallower structural levels, within top Albian-to-Miocene overburden, the faults offset
249 normal and thrust faults (Figs 5 and 6). Finally, at the top Miocene, several deep-water channels
250 represent piercing points (CH1a-e; Figs 5c and 6e-f). Strike-slip faults thus divide the salt and
251 overburden into six sub-domains that are principally characterised by differing styles and
252 magnitudes of salt-related deformation (Figs 5, 9 and Table 1).

253 Having described the two-dimensional geometry of the salt-detached strike-slip faults, we now
254 describe and interpret the three-dimensional geometry and kinematics of the four largest and best-
255 imaged faults.

256

257 **5.2 Along-strike variations in lateral offset and throw**

258 We use various salt- and channel-related piercing points at top salt and Albian-to-Miocene to
259 determine along-strike changes in lateral offset along the strike-slip faults (Figs 4b, 5-6), showing
260 this varies from 100-1683 m (purple dotted line in Fig. 8). Offset vs. distance plots are generally

261 characterized by up to four fault arrays (labelled 1-4; Fig. 8). Each array is defined by either a
262 symmetric or an asymmetric distribution of offset, defined by either a flat-topped profile, such as
263 second array in F3a, or a peaked profile, such as second array in F1a. In general, however,
264 maximum lateral offsets occur near the fault centres, decreasing to the lateral tips, where faults
265 may physically link with adjacent structures. Lateral offset (strain) gradients range from 0.09-0.76,
266 which are within the range of those reported for normal faults in the British coalfields (0.001-
267 0.067; see Walsh and Watterson, 1989 and Nicol et al., 1996) and imaged in seismic reflection
268 data (0.007-1.05; see Nicol et al., 1996, Jackson and Rotevatn, 2013 and Tvedt et al, 2016).

269 We record throw at the top of Albian, Eocene, and Upper Miocene structural levels (Fig. 8).
270 Plotting throw against along-strike distance reveals multiple negative and positive values, which
271 reflects normal and reverse throws, and that define individual segments (see above). These
272 segments have a maximum throw of up to 800 m and are defined at their lateral tips by throw
273 minima. Throw gradients range from 0.10—6.3, being highest where a segment defined by normal
274 throws passes into one defined by reverse throws, or vice versa. Throw vs. distance plots are either
275 symmetrical and defined by a well-defined throw maxima (i.e., a peak; e.g. label 11f in Fig. 8a),
276 or asymmetric and flat-topped (e.g. label 11f in Fig. 8b). Some plots show a gap between these
277 various throw patterns due to the presence of salt diapirs (i.e. wall) or weld (e.g. label 11b in Fig.
278 8b and label 11af in Fig. 8h). Maximum throw (d_{\max}) typically occurs at the top of the Albian, or
279 more rarely at the top of the Eocene or Upper Miocene, in particular near areas of diapirism or
280 welding (Fig. 8). To constrain how throw varies both along-strike and vertically upwards, into
281 younger strata, we use selected inflection points on the lateral offset vs. distance plot, and distinct
282 changes in throw at the Albian level (i-xix; Fig. 8), given this level defines the top of pre-kinematic
283 strata and thus records most if not all of the strike-slip related strain (Erdi and Jackson, 2021).

284

285 **5.3 Vertical variations in throw**

286 Tz plots illustrate vertical variations in throw at specific positions on the strike-slip faults (Fig.
287 11). The plots are characterized by broadly asymmetric distribution profiles along strike. These
288 profiles consist of up to two throw maxima, defined by either normal or reverse throws, and that
289 are typically located: (a) near the top of the Albian (labelled 1 in Fig. 11); (b) near the top of the
290 Eocene or intra-Eocene (labelled 2 in Fig. 11); and, where F1 and F4 are close to the SW2 and

291 SW4; or, (c) the top of the Lower and Upper Miocene (labelled 3 for F1 and F4 in Fig. 11). These
292 two throw maxima are separated by a polarity reversal (i.e. normal to reverse throw, or vice versa)
293 and a throw minima, which typically occurs in intra-Eocene strata and near the top of the
294 Oligocene, respectively.

295 From the lower throw maxima downward to the top of salt, we speculate that the throw values
296 gradually decrease, with any strain within the salt being diffuse (dotted line in Fig. 11). Upwards
297 from the upper throw maxima, the style of throw decrease varies along strike of individual faults,
298 depending on the structural level at and the manner in which the fault tips out (i.e. the fault tips
299 out within younger strata seaward and/or links with a salt wall and weld; see above). Overall,
300 however, we observe that the throw gradients above where polarity reversals occur are high (0.23-
301 1.92; e.g. Fig. 11c, l, u), whereas those above throw minima or toward upper tip are relatively low
302 (0.08-to-1.42) (e.g. Fig 11g, h, ac).

303

304 **5.4 Spatial and geometric relationship between strike-slip faults and base-salt relief**

305 The salt-detached strike-slip faults vary in terms of their spatial relationship with base-salt
306 relief. Although some parts of these faults overlie areas where the base-salt is relatively flat, such
307 as the southwestern end of F2a, many faults strike sub-parallel to NE-trending ramps or the more
308 elliptical base-salt highs (Figs 4c and 8). The faults also display varying degrees of physical linkage
309 with the underlying base-salt relief, with some apparently being hard-linked (Figs 10c-f and 11).
310 A key observation of the relationship between base-salt relief and the overlying strike-slip faults
311 is that the maximum throw for each fault, whether located at the top of the Albian or Eocene, are
312 *presently* and broadly underlain by the NE-trending ramps (e.g. label 10d in Fig. 8a and 11O in
313 Fig. 8b).

314

315 **5.5 Strike-slip fault-related thickness variations and their relationship with throw**

316 We see four key thickness patterns in the overburden adjacent to a strike-slip fault array and its
317 associated structures. The first pattern is defined by several, up to 1.4 km thick and 4 km long
318 depocenters that broadly trend perpendicular to and are intersected by, the strike-slip faults (white
319 dotted lines in Fig. 7). These patterns include some ramp syncline basins (RSBs of Evans and
320 Jackson, 2019; Fig. 7d) that differ in size across the faults, and that therefore likely record different

321 rates and magnitudes of overburden translation seaward. The second pattern is defined by areas of
322 stratal thinning that are up to c. 0.3 km thick and c. 2.5 km long, and that trend broadly parallel to
323 the strike-slip faults (green dotted lines in Fig. 7a-c, d, f). More specifically, these areas overlie
324 pop up-like structural highs, which likely reflect local contraction along a restraining bend in the
325 fault (Fig. 8) (e.g. Cunningham and Mann, 2007). This pop up-related thinning is located where
326 normal throw passes into reverse throw, and near an inflection point in the style of lateral offset.
327 The third pattern is characterised by several fault-parallel depocenters that are c. 0.6-1.4 km thick
328 and up to 12 km long, and which are bound by a main strike-slip fault segment and an antithetic
329 fault (F2a and F4a-c; light blue dot line in Fig. 7c, g, h). This depocenter locally spans areas of
330 normal throw on segments identified at either the Eocene or Miocene structural level (Fig. 8). We
331 interpret this depocenter as a transtension-related, pull-apart basin developed at releasing stepovers
332 (e.g. Sylvester, 1988; Mann, 2007). The fourth pattern is defined by several, c. 0.25-1.4 km thick
333 and up to c. 2 km long, N-trending depocenters that are flanked by the normal fault-dominated
334 splay zones between F1 and F2, or at the lateral tip of F4a. We interpret that these depocentres
335 record growth of these extensional splays and thus the related strike-slip fault segments (labelled
336 'i' ; Fig. 7c, e, f) (e.g. Kim et al., 2004; Peacock and Sanderson, 1995).

337 The distribution of these types of depocenters and the thickness variations that define them
338 record the growth of strike-slip fault array and associated structures. Albian thickness maps show
339 that the fault-intersected depocenters and pop up-related thinning span 34-65% of the present trace
340 lengths of F2a and F3 (Fig. 7a-b). In contrast, these types of thickness variations are only locally
341 developed (up to 18% of the present trace length) along the F1a and F4a (Fig. 7b). Eocene-
342 Oligocene thickness maps show that the fault-intersected depocenters and pop up-related thinning
343 are broadly distributed along F1-F4a, indicating the related faults were growing at this time (Fig.
344 7c-f). However, thickness patterns in the Eocene-Oligocene strata differ to those in the underlying
345 (i.e. older) Albian strata in two key ways: (i) distribution of the fault-intersected depocenters and
346 pop up-related thinning decreases from up to 65% along F2a and F3 to only a maximum of 33%
347 along F3a upwards into the Oligocene interval; and, (ii) the extensional stepover-related
348 depocenters that are distributed between F1-F2 and F4, reflecting activity of the splay zone. Upper
349 Miocene-Seabed thickness map show a distinctive transtension-related depocenter that spans up
350 to 59% and 87% of the present traces of F1 and F4a-b, respectively (Fig. 7g-h). These maps also
351 show that Upper Miocene-Seabed strata thin towards salt walls SW2 and 4.

352 EI profiles provide further, quantitative insights into overburden thickness patterns both along-
353 strike and down-dip of the strike-slip faults. We observe that EI values >1 (i.e. thickening-into-
354 the-hanging wall) are correlate with areas of normal throw (label i; Fig. 11), whereas values <1
355 (thickening-into-the-footwall) correlate with areas of reverse throw (label ii; Fig. 11). EI values
356 >1 also occur where reverse throws are observed (label iii; Fig. 11); in this case we interpret that
357 rather than demonstrating either stratigraphic thickening or thinning into the hangingwall of a
358 (dipping) strike-slip fault, as shown by the overburden map (Fig. 7), these values reflect the across-
359 fault juxtaposition of differing thickness in depocentres due to strike-slip faulting.

360 Thickness variations associated with the fault arrays reveal that they were active at different
361 times (Figs 7 and 11). The fault arrays were active since at least c. 100.5 Ma (Albian), with F2a
362 and F3 active until c. 23 Ma (Oligocene), and F1a and F4a-b still being active.

363

364 **6. Origin and evolution of strike-slip fault systems in the Outer Kwanza Basin**

365 Having described: (a) the geometry of the strike-slip faults and their relationship with base-salt
366 relief, and salt- and other salt-related overburden structures; and (b) thickness changes in related
367 growth strata, we now consider the origin of these structures, before reconstructing their evolution.
368 Key to this is our ability to backstrip throw on the faults, which thus allows us to plot fault growth
369 trajectories (i.e., throw-distance relationships through geological time) (e.g. Chapman and
370 Meneilly, 1991, Dutton and Trudgill., 2009; Tvedt et al., 2016).

371

372 **6.1 Nucleation of the salt-detached strike-slip fault arrays and the role of base-salt relief**

373 Erdi and Jackson (2021) argue that the Cretaceous-Neogene strike-slip fault array in the Outer
374 Kwanza Basin are physically detached (due to the presence of Aptian salt) from the NE-trending,
375 transform-related base-salt relief. This is consistent with our Tz analysis, showing that maximum
376 throw on many of the strike-slip fault segments is located near the top Albian or shallower (Fig.
377 11). In terms of the trigger for fault nucleation, we suggest the following: (a) originally thin salt
378 on the NE-trending base salt high flowed seaward more slowly than the thick salt next to the high
379 (see variable salt flux across dip-parallel base-salt relief in the physical models of Dooley et al.,
380 2017); and/or; (b) different seaward translation rate across the faults (Fig. 5; Erdi and Jackson,

381 2021). The former interpretation cannot be conclusively resolved by our study because of the
382 *present* spatial relationship between the salt-detached strike-slip faults and base-salt relief is highly
383 unlikely to reflect their relationship when the fault was formed, given salt and its overburden
384 flowed seaward by at least 13 km after fault nucleation in the Albian (Fig. 4c; Erdi and Jackson,
385 2021). Although the former interpretation is plausible, the latter interpretation has at least been
386 clearly demonstrated in our study area, suggesting that different seaward translation rate already
387 occurred perpendicular to the array of strike-slip faults in Albian (i.e. the initial 11-13% of their
388 fault histories; Fig. 12). Thus, fault nucleation likely occurred updip to the NE, outside of the
389 present study area (sensu Erdi and Jackson, 2021). Furthermore, the fact that the faults appeared
390 to nucleate near the top of the Albian interval, some distance (i.e. at least 800 m) above and yet
391 parallel to the NE-trending ramp, suggest that after forming, these faults propagated downward
392 into and through the salt, in some places then coincidentally linking with underlying base-salt
393 highs.

394

395 **6.2 Growth of the strike-slip fault array**

396 Having established: (i) the geometry of the strike-slip fault array; (ii) the present relationship
397 between the faults within this array, and spatially related salt structures and base-salt features (e.g.,
398 ramps); and (iii) that the faults nucleated near the top of the Albian and are thus post-Albian, we
399 now reconstruct the growth history of the salt-detached strike-slip faults using thickness patterns
400 in growth strata and the fault geometries.

401

402 **6.2.1 Late Albian (113-100.5 Ma)**

403 Until at least c. 100.5 Ma, the constituent segments of F1a-F4a were physically isolated from
404 one another (i, iv and xii-xix), whereas some segments had linked to form a through-going, strike-
405 slip fault array (ii-iii and vii-x; Fig. 12 and Fig. 13a). Segment linkage was associated with the
406 formation of restraining bends, recorded by areas of pop up-related thinning (Fig. 7, and green
407 colour at 113-100.5 Ma; Figs 12a and 13a). As a result of these kinematics, the fault array was
408 associated with coeval normal and reverse slip.

409

410 6.2.2 Late Cretaceous-Paleogene (100.5-23 Ma)

411 During the first part of this period, from the Late Cretaceous until the Eocene (from 100 to 34
412 Ma; i.e. capturing 69-81% of the total slip history of the faults), the constituent segments (i-xvi
413 and xix) of F1a-F4a continued to grow by vertical and lateral propagation of their tips. Fault growth
414 involved both dip and strike linkage (orange colour of ii-xvi and xix; Fig. 14a-d; see also at 34 Ma;
415 Fig. 12 and BP and RL; Fig. 13b), or via tip propagation of a single structure (which may not have
416 reached the free surface) through the overburden, similar to that documented for normal faults (e.g.
417 Baudon and Cartwright, 2008). The interpretation that some faults never reached the free surface
418 is supported by the constant low throw gradient (<1.00) observed near the upper tips of some
419 segments (e.g. Fig. 11e, f), whereas the occurrence of dip linkage is supported by the observation
420 of multiple throw maxima at Eocene and near Albian structural level (Fig. 11 c, l, u, y). Some
421 throw maxima at the Eocene structural level are defined by normal offsets (Fig. 11 l, u, y),
422 indicating the established segments formed during the Albian dip-linked with overlying
423 extensional faults at this time (RL on F2a; Fig. 13). Locally, however, reverse throw maxima are
424 observed at this structural level (Fig. 11c), located near an area of pop up-related thinning in the
425 Eocene (Figs 7c-d and label 11c; Fig. 8). These observations suggest the strike-linkage of segments
426 was associated with restraining bend-related deformation, involving; (i) local uplift of a formerly
427 normal fault-bounded block; and (ii) dip-linkage between deep faults with normal throw and
428 shallower faults with reverse throws (RL on F1a; Fig. 13).

429 A few new segments also nucleated along F4a during this time (xvii-xviii; Figs 12d and 13b),
430 whereas F2a and F3 had accumulated their near present-day lengths. Growth and linkage of the
431 constituent segments of F2a, led to the formation of an extensional stepover and associated
432 transtension related-depocenters (Figs 7c, and at 34 Ma in Fig. 12b). Given the presence of
433 associate depocenter (Fig. 7c), the growth and overlap of F1a and F2a in the Eocene resulted in
434 the formation of a extensional fault-dominated splay zone or relay between them (splay zone; Fig.
435 13b). During the Eocene-Oligocene (from 34 to 23 Ma; i.e. capturing 79 and 92% activity of the
436 total F1a and F4a, and F2a-F3 history, respectively), many fault segments became inactive, with
437 only a few (and a related transtensional depocentre) along and at the tip of F4a, and along the
438 southern portion of F1a and F3, remaining active (Figs 7e-f and 11).

439

440 **6.2.3 Miocene-Recent (23-0 Ma)**

441 By the Miocene (from c. 23 to 5.3 Ma), F2a and F3 were inactive and had been buried by
442 younger, post-rift sediment (Fig. 13c). In contrast, during this 17.7 Ma periods (capturing 95%
443 activity of the total fault histories), the established segments along F4a-b and the southern portion
444 of F1a continued to grow to their near present-day lengths, with several new segments forming
445 after 5.3 Ma (Figs 12a, d and 13c). The distribution of throw at the Albian level, which records the
446 cumulative displacement on the faults through time, reveal that these established segments grew
447 by solely lateral lengthening via tip propagation (ii-iv) and/or increasing in their maximum throw
448 (v-vi, xvii-xix) (Fig. 12a, d and purple colour; Fig. 14a, d). As shown by multiple throw maxima
449 at Albian or Eocene, and Miocene structural level (Fig. 11g-h and ab-ae), the maximum throw at
450 the Miocene are interpreted to be related to dip-linkage reactivation due to nucleation of new fault
451 segments at this strata. Given Upper Miocene-seabed strata thin toward salt diapirs SW2 and SW4
452 (Figs 7g-h), we suggest that fault reactivation reflect Miocene salt diapirism. This interpretation is
453 supported by the structural restoration presented by Erdi and Jackson (2021), who show that SW2,
454 which flanks F4a-b, underwent extension-driven fall and active rise after the Miocene. However,
455 sinistral offsets are observed on some channels at top Upper Miocene (Figs 5c and 6e-f), thus dip-
456 linkage related reactivation likely was contemporaneous with horizontal (i.e. translation) salt
457 tectonic movement during Miocene. Subsequently, by the Miocene-Recent (last 5.3 Ma; i.e. last
458 5% of the total fault history), segment growth and/or diapirism induced the formation of
459 transtensional graben, as clearly reflected by the formation of Miocene-seabed depocenters along
460 the faults (Fig. 7g-h).

461

462 **7 Discussion**

463 **7.1 Geometry and growth model of strike-slip faults**

464 Numerous studies have focused the two-dimensional, typically map-view structure and related
465 kinematics of strike-slip faults in various tectonic settings (e.g. Cunningham and Mann, 2007;
466 Mann, 2007), with 2D seismic reflection data or single profiles from 3D volumes being used to
467 illustrate their two-dimensional geometry (e.g. Harding, 1985; 1990; Leduc et al., 2012). Because
468 of this, the three-dimensional geometry and related kinematic development of the strike-slip faults
469 is poorly understood compared to, for example, normal faults (see reviews by Childs et al., 2017

470 and Rotevatn et al., 2019). Some field-based studies have described the four-dimensional patterns
471 of strike-slip faulting, but again, due to outcrop limitations, these have largely focused on map-
472 view patterns of, for example, throw; they have not, therefore, been able to directly deduce related
473 dip-slip motions, or the dynamics of tip propagation and related fault linkage (Peacock, 1991; Kim
474 et al., 2000; 2001; Nixon et al., 2011).

475 Three-dimensional seismic reflection data have relatively recently been employed to highlight
476 the strike- and dip-slip components of motion on strike-slip faults. For example, Benesh et al.
477 (2014) use 3D seismic reflection data from the Niger Delta to resolve the kinematics of shale-
478 detached strike-slip faults by mapping piercing points (i.e. deep-water channels and pre-existing
479 thrust faults). They produced along-strike slip profiles by conducting map view-based surface
480 restorations, revealing that strike-and dip-slip offsets and throws are not uniform along the faults.
481 They did not, however, investigate the long-term kinematics of the faults. Deng et al (2019) use
482 spatial variations in throws to determine the four-dimensional patterns of slip on segmented, strike-
483 slip faults overlain by *en echelon* normal faults. They propose a model involving the growth of
484 strike—slip faults by upward propagation of their tips and linkage with overlying faults.

485 Physical models have also been used to explore the kinematics of strike-slip faults above a
486 crustal weak zone, showing that they initially formed segmented arrays of Riedel shear-like
487 structures that propagated laterally and eventually hard-linked, resulting in the formation of
488 restraining and/or releasing stepovers or bends (e.g., Dooley and Schreurs, 2012). More recently,
489 Dooley et al. (2017) illustrate the formation, geometry, and kinematics of salt-detached strike-slip
490 faults, showing that during basinward flow of salt and its overburden, different salt thicknesses
491 across dip-parallel base-salt relief can generate parallel strike-slip faults in the overburden. The
492 strike-slip faults form when the overburden is relatively thin, separating the faster translating,
493 relatively thick salt domain from slower moving, relatively thin salt domain.

494 We used 3D seismic reflection data from the Outer Kwanza Basin, offshore Angola to determine
495 the geometry and kinematics of salt-detached strike-slip fault arrays. Growth strata clearly indicate
496 these structures nucleated in the Albian; however, the trigger for fault formation is less clear, given
497 these structures likely formed 13-23 km updip of their present location, being subsequently
498 translated seaward into their present positions. However, drawing on observations from physical
499 models (Dooley et al., 2017) and other salt basins (e.g. Rowan et al., 1999; Fort and Brun, 2012),

500 we speculate that the strike-slip faults formed to accommodate variable rates and magnitudes of
501 overburden translation, related to base-salt related variations in salt thickness.

502 Using 3D seismic reflection data from the Outer Kwanza Basin, offshore Angola and a range
503 of qualitative (i.e., isopach) and quantitative (i.e. lateral offset vs. distances and throw vs. distance
504 and -depth plots, throw backstripping) fault analysis techniques, we are able to constrain the
505 geometry and growth of a salt-detached strike-slip fault array. We show that these arrays initially
506 consisted of several geometrically separate segments along which throw varied between normal
507 and reverse motions (Fig. 8), consistent with the observations of Benesh et al (2014). These
508 segments grew laterally via tip propagation, eventually linking with neighbouring segments (Fig.
509 12). Similar kinematics have been described from field-based studies (e.g. Peacock, 1991; Kim et
510 al., 2000), and are simulated in physical models (e.g. Dooley and Schreurs, 2012). However, the
511 excellent imaging and spatial coverage provided by our 3D seismic reflection dataset mean we are
512 also able to show the key role played by dip-slip motions, and how these relates to the map-view
513 evolution of the arrays, something that is difficult to do in exposures permitting only a 2D view of
514 fault geometry (e.g. Peacock, 1991; Kim et al., 2000; 2001; Nixon et al., 2011). Our study shows
515 that the evolution of these arrays was associated with the nucleation, and dip and strike propagation
516 and linkage of segments experiencing coeval normal and/or reverse slip (Figs 12). Furthermore,
517 throw-depth plots clearly show the upper tips of individual segments are characterised by
518 consistently low throw gradients (Fig. 11e-f, m-n and z-aa), suggesting they were reactivated at
519 some point in their history, and were not surface-breaching. This interpretation is consistent with
520 that of Deng et al (2019), who also show that strike-slip faults need not always be surface-breaking.
521 However, the presence of multiple throw maxima on throw-depth plots (Fig. 11c, g-h, l, u, y, ab-
522 ae) suggest faults were also able to increase their height via reactivation and dip linkage with
523 structures newly forming within shallower host rock.

524

525 **7.2 Strike-slip fault scaling**

526 Figure 14e shows a plot of lateral maximum displacement-trace distance data for a global
527 compilation of strike-slip faults, including the lateral offset presented here from the Outer Kwanza
528 Basin (Fig. 8). Our data fills a scale gap in the previous, global dataset (i.e., displacements of 10^2 -
529 10^3 m and distances of 10^3 - 10^4 m), lying within the overall scatter of these existing data. The scatter

530 observed in our study may reflect measurement errors, sampling bias, and/or variations in the
531 mechanical stratigraphy of the host (e.g. Kim and Sanderson, 2005; Torabi and Berg, 2011),
532 although our backstripping results suggest it is a function of the growth or more specifically, the
533 propagation and linkage history of the strike-slip faults (c.f. Cartwright et al., 1995) (Fig. 12). Our
534 analysis of how throw and distance (and their associated scaling relationship) change through time
535 consistently show that the constituent segments (ii-xix) of the strike-slip fault arrays either: (i)
536 attained their near-final lengths early during deformation, associated with lateral tip propagation
537 and the linkage of adjacent segments (i.e., consistent with the constant-length model proposed for
538 normal faults; e.g. Walsh et al., 2002) (label a; Fig. 14a-c); or (ii) grew via broadly synchronous
539 increases in throw and length (i.e., consistent with the propagating fault model proposed for normal
540 faults; e.g. Walsh and Watterson, 1988; Dawers et al., 1993) (label b; Fig. 14a-d). These
541 observations suggest that scatter in the scaling relationships for strike-slip faults may simply reflect
542 the fault growth process, in a similar way to that proposed for normal faults (e.g. Walsh and
543 Watterson, 1988; Walsh et al., 2002).

544

545 **8 Conclusions**

546 We used 3D seismic reflection data from the Outer Kwanza Basin, Offshore Angola to
547 determine the three-dimensional geometries and kinematics of salt-detached strike-slip faults. We
548 show that deformation of Albian-to-Recent overburden above Aptian salt is locally accommodated
549 by four, NE-SW-striking arrays that are up to 13 km long, 0.8 km tall, and which have normal and
550 reverse throws of up to 617 m and 830 m, respectively. We speculate that these faults formed to
551 accommodate along-strike variations in the rates and magnitudes of the salt-detached, seaward
552 translation of overburden, possibly related to base-salt relief and related variations in salt thickness.
553 Regardless of their origin, we show that the strike-slip arrays can be divided into several segments,
554 defined by along-strike changes in the sense of throw, from normal to reverse. Our kinematic
555 analysis reveals that faults nucleated sometime in the late Albian, with some segments establishing
556 their near-final lengths during the initial 69% of their faulting history), whereas others attained
557 their present-day length much later (i.e., after 95% of their faulting history). Fault growth, map-
558 view changes in fault strike, and along-strike changes from normal to reverse throws resulted in
559 the formation of releasing stepovers and restraining bends, whereas dip-slip motions resulted in

560 fault reactivation and dip-linkage. The present-day throw-distance scaling relationships for the
561 Outer Kwanza Basin fault arrays lie within the overall scatter of a global dataset, with some of the
562 scatter within our dataset likely reflecting the fault growth process, in a similar way to that
563 documented for normal faults. Our study provided a natural example of the geometry and
564 kinematics of strike-slip faults on a salt-bearing passive margin, showing the integral roles of
565 strike- and dip-linkage in their development. These learnings may be applicable to similar faults
566 forming within intraplate settings.

567

568 **Acknowledgement**

569 We wish to thank Joe Cartwright, Mark Rowan, Stefan Back, Rebecca Bell, Timothy Wigan
570 and Bailey Lathrop for discussions during the course of this study. A big thank you to CGG for
571 providing access to the high-quality 3D seismic dataset and for allowing publication of the results
572 of this study. This study is a PhD study of the first author, who is sponsored by Indonesia
573 Endowment Fund for Education/Lembaga Pengelola Dana Pendidikan (LPDP). The first author
574 would also like to thank the Research Center for Geotechnology, Indonesian Institute of Science
575 (LIPI) (now National Research and Innovation Agency - BRIN), Indonesia for indirect assistance
576 and administrative support during his PhD research. All authors acknowledge Schlumberger for
577 providing Petrel software to Imperial College London.

578

579 **Table Captions**

580 Table 1: Summary of structural and stratigraphy features defining the overburden sub-domains,
581 separated by salt detached strike-slip faults (see Figure 5).

582 **Figure Captions**

583 **Figure 1:** Schematic diagrams illustrating the geometry and kinematics of salt-detached strike-
584 slip faults. (a) A synoptic model (modified from Rowan et al., 1999). (b) An example from the
585 Levant Basin, offshore Israel (modified from Cartwright et al., 2012). (c) An example from the
586 northern Gulf of Mexico (Rowan et al., 1999). (d) An example from the northern Gulf of Mexico
587 (modified from Fort and Brun, 2012). (e) An example from a physical model, highlighting the

588 key role on base-salt relief and salt thickness on fault development and geometry (modified from
589 Dooley et al., 2017).

590 **Figure 2:** A simplified map and cross section of the Offshore Angola region, with the
591 approximate location of our study area indicated by the red box. (a) A regional map illustrating
592 the key tectonic features and salt tectonic domains in the Offshore Angola. (b) A semi-regional
593 cross-section showing the presence of salt-detached strike-slip faults above the Aptian salt layer.
594 The salt layer is confined by an underlying, rift-related structural high (SH) and a crustal-scale
595 transfer fault zone (modified from Erdi and Jackson, 2021).

596 **Figure 3:** Schematic diagram illustrating the nomenclature and techniques used to determine the
597 geometry of strike-slip faults in this study. (a) oblique view of a strike-slip fault; (b)
598 displacement contours on a fault surface; (c) a lateral offset vs. throw displacement profile; (d) a
599 schematic two-dimensional cross-section through a strike-slip fault; (e) a throw-depth profile
600 across a fault; (f) an expansion indices plot.

601 **Figure 4:** Uninterpreted and interpreted of (a) base-salt, and (b) salt thickness maps. Both (a) and
602 (b) are overlaid to create (c), a composite sketch map showing how salt thickness and base-salt
603 depth relate. These maps illustrate that salt anticlines (SA), wall (SW), squeezed walls (SQ), and
604 anticlines (SN), and salt-detached strike-slip fault arrays *presently* occur parallel to and above
605 NE-, N-, NE-trending base-salt relief (ramps).

606 **Figure 5:** Uninterpreted and interpreted variance attribute maps at (a) the top of Albian, (b) the
607 top of Eocene, and (c) the top of Miocene structures, illustrating the geometry of several strike-
608 slip fault arrays (F1-F5) at each structural level. Note that these arrays define the margins of
609 structural domains defined by different styles and intensities of salt-related deformation (see
610 Table 1 for full description of each zone). Seismic data courtesy of CGG Earth data (previously
611 CGG Multi-Client).

612 **Figure 6:** Zoom-in of a variance map, showing the detailed geometry of NE-trending, salt-
613 detached strike-slip faults (F1-F4) between the (a-b) Albian, (c-d) Eocene, and (e-f) Upper
614 Miocene structural levels (see map location shown in Figure 5; see also Figure S4-S5 in
615 Appendix C for uninterpreted and interpretative sketch of variance attribute maps). Seismic data
616 courtesy of CGG Earth data (previously CGG Multi-Client).

617 **Figure 7:** Interpreted isopach maps (contour interval of 100 m) for the (a-b) Aptian-Albian, (c-d)
618 Albian-Eocene, (e-f) Eocene-Oligocene, (g-h) Upper Miocene to seabed intervals, showing
619 thickness patterns adjacent along the strike-slip fault arrays (F1-F5) and significant salt structures
620 (SW2 and SW4) (see map location in Figure 5; see also Figure S6-S7 in Appendix C for
621 uninterpreted and interpretative sketch of isopach maps).

622 **Figure 8:** Composite thickness variation (derived from isopach maps; see Fig. 7) and
623 displacement-distance graphs for strike-slip faults (a) F1a, (b) F2a, (c) F3, and (d) F4a, b (see
624 Table S1-S2 in Appendix D for raw data of displacement-distance). The displacement-distance
625 graphs consist of two plots; maximum lateral offset (LO; right side) and throw (TH; left side).
626 The maximum lateral offsets (purple color) are constrained by piercing points (i.e. salt diapir,
627 anticline and channels), whereas throws are constrained by the vertical separation of the Albian
628 (blue), Eocene (orange), and Upper Miocene (yellow) seismic reflections. The location of
629 prominent base-salt relief is shown in black. The locations of pop up-related stratal thinning and
630 transtension-depocenters (as defined on Albian, Eocene and Upper Miocene isopach maps; see
631 Fig. 7) are also shown, reflecting the distribution of restraining bends and releasing stepovers
632 along the faults.

633 **Figure 9:** Seismic profiles across each strike-slip fault-bound structural domain (profile locations
634 shown in Figures 4a, b and 5a; see also Figure S2 in Appendix B for uninterpreted cross
635 sections) (Erdi and Jackson, 2021). (a) salt anticlines (SA4-6) in the northwest of the study area;
636 (b) a squeezed salt anticline (SN1b), wall (SQ1), and roller (unnamed) in the center of the study
637 area; (c) salt anticlines (SA1-3), a squeezed wall (SQ2a), and a roller (unnamed) in the center of
638 the study area; (d) fore- and back-thrusts above a squeezed salt wall (SQ2b), and a reactive salt
639 wall (SW2). Seismic data courtesy of CGG Earth data (previously CGG Multi-Client).

640 **Figure 10:** Seismic profiles illustrating the two-dimensional structural style of salt-detached
641 strike-slip faults arrays (F1-F4) (profile locations shown in Figures 4a, b, 5a and 8; see also
642 Figure S3 in Appendix B for uninterpreted cross sections). (a) F1a, showing a planar cross-
643 sectional geometry and normal throws above a primary weld. (b) F1a in a more seaward (i.e.,
644 south-westerly) position compared to (a), showing normal throws at the Albian structural level,
645 but reverse throws at the Eocene structural level. (c) F1a in a more seaward (i.e., south-westerly)
646 position to (b), displaying reverse throws at all structural levels; F2a is planar and displays

647 normal throws. (d) 0.5 km seaward of (c), F1a and F2a display normal throws and bound
648 negative flower structures. (e) 2 km seaward of (d), F1a displays reverse throws, whereas F2a
649 persistently display negative flower structures. (f) F3, showing a planar cross-sectional geometry
650 and normal throws at Albian-Lower Miocene structural levels; F4a bounds negative flower
651 structures and normal throws at Albian-Seabed structural levels. (g) 3.6 km seaward of (f), F4 is
652 defined by soft-linkage between F4a and F4b, and the oppositely dipping (i.e., antithetic) array,
653 F4c. Note that the strike-slip faults are located above either base-salt highs or areas in which the
654 base-salt is flat. Seismic data courtesy of CGG Earth data (previously CGG Multi-Client).

655 **Figure 11:** Throw-depth (T-z) and corresponding expansion indices plots for the (a-i) F1a, (j-r)
656 F2a, (s-aa) F3, and (ab-ag) F4a arrays (see their corresponding location on displacement-distance
657 in Fig. 8). The location of maximum throw is labelled (label 1-3). Note that throw varies along-
658 strike and the faults upper tips are characterized by low throw gradients. EI plots show a broadly
659 positive correlation between EI values >1 (i.e. thickening-into-the-hangingwall) and areas of
660 normal throw (labelled “i”), and EI values <1 (thickening-into-the-footwall) and areas of reverse
661 throw (labelled “ii”). Areas where EI values >1 are associated with reverse throws are also seen,
662 with this inferred to record the across-fault juxtaposition of depocenters due to strike-slip
663 motions on faults bounding previously geographically separate depocentres (labelled “iii”).

664 **Figure 12:** Backstripping of composite throw-distance and isopach maps for (a) F1, (b) F2, (c)
665 F3 and (d) F4 array. Note that these backstripping data show the evolution of throw at the top
666 Albian structural level, illustrating the formation of restraining bends and releasing stepovers
667 (taken from Figure 7) at 100.5 Ma (i.e., after 11-13% of the faulting history), 34 Ma (i.e., after
668 69-81% of the faulting history), and 5 Ma (i.e., after 95% of the faulting history). Backstripping
669 used the maximum throw subtraction method (e.g. Rowan et al., 1998; see also Appendix A2 for
670 full explanation).

671 **Figure 13:** Schematic map-view and cross-sectional reconstruction showing the interpreted
672 evolution of strike-slip faults arrays at (a) 100.5 Ma, (b) 34 Ma, and (c) 5 Ma.

673 **Figure 14:** Throw-distance trajectory plots for (a) F1a, (b) F2a, (c) F3, and (d) F4 since 100.5
674 Ma (see each segment in Fig. 8 and their corresponding evolution in Fig. 12). In (e) we plot our
675 lateral offset vs. displacement data from array of F1-F4 against a global dataset of lateral
676 displacement-length for strike-slip faults (see Table S3 in Appendix D for raw data) (McMillan,

677 1975; Wesnousky, 1988; Scholtz and Cowie, 1990; Peacock, 1991; Kim et al., 2000; Sieh and
678 Natawidjaja, 2000; Jachens et al., 2002; Walker and Jackson, 2002; Tatar et al., 2004; Rovida
679 and Tibaldi, 2005; Nemer and Meghraoui, 2006; Fu and Awata, 2007; de Joussineau and Ayidin,
680 2009). The inset shows a zoom-in of the lateral offset vs. distance.

681

682 **Data Availability Statement**

683 The seismic data supporting the findings of this study are available from CGG. However,
684 restrictions apply to the availability of these data, which were used under license for this study.

685

686 **References**

687 Bahorich, M., & Farmer, S. (1995). 3-D seismic discontinuity for faults and stratigraphic
688 features: The coherence cube. *The Leading Edge*, 14(10), 1053-1058. doi:10.1190/1.1437077

689 Bates, R. L., & Jackson, J. A. (1997). *Glossary of geology*. Alexandria, Virginia: American
690 Geological Institute.

691 Baudon, C., & Cartwright, J. (2008). The kinematics of reactivation of normal faults using high
692 resolution throw mapping. *Journal of Structural Geology*, 30(8), 1072-1084.

693 doi:10.1016/j.jsg.2008.04.008

694 Benesh, N. P., Plesch, A., & Shaw, J. H. (2014). Geometry, kinematics, and displacement
695 characteristics of tear-fault systems: An example from the deep-water Niger Delta. *AAPG*
696 *Bulletin*, 98(3), 465-482. doi:10.1306/06251311013

697 Bergen, K. J., & Shaw, J. H. (2010). Displacement profiles and displacement-length scaling
698 relationships of thrust faults constrained by seismic-reflection data. *GSA Bulletin*, 122(7-8),

699 1209-1219. doi:10.1130/B26373.1

700 Bull, S., Cartwright, J., & Huuse, M. (2009). A review of kinematic indicators from mass-
701 transport complexes using 3D seismic data. *Marine and Petroleum Geology*, 26(7), 1132-1151.

702 doi:<https://doi.org/10.1016/j.marpetgeo.2008.09.011>

703 Cartwright, J., Jackson, M., Dooley, T., & Higgins, S. (2012). Strain partitioning in gravity-
704 driven shortening of a thick, multilayered evaporite sequence. *Geological Society, London,*
705 *Special Publications*, 363(1), 449.

706 Cartwright, J., Bouroullec, R., James, D., & Johnson, H. (1998). Polycyclic motion history of
707 some Gulf Coast growth faults from high-resolution displacement analysis. *Geology*, 26(9), 819.
708 doi:10.1130/0091-7613(1998)026<0819:pmhosg>2.3.co;2

709 Cartwright, J. A., Trudgill, B. D., & Mansfield, C. S. (1995). Fault growth by segment linkage:
710 an explanation for scatter in maximum displacement and trace length data from the Canyonlands
711 Grabens of SE Utah. *Journal of Structural Geology*, 17(9), 1319-1326. doi:10.1016/0191-
712 8141(95)00033-a

713 Chapman, T. J., & Meneilly, A. W. (1991). The displacement patterns associated with a reverse-
714 reactivated, normal growth fault. *Geological Society, London, Special Publications*, 56(1), 183-
715 191. doi:10.1144/gsl.sp.1991.056.01.12

716 Childs, C., Holdsworth, R. E., Jackson, C. A. L., Manzocchi, T., Walsh, J. J., & Yielding, G.
717 (2017). Introduction to the geometry and growth of normal faults. *Geological Society, London,*
718 *Special Publications*, 439. Retrieved from
719 <http://sp.lyellcollection.org/content/early/2017/09/05/SP439.24.abstract>

720 Christie-Blick, N., & Biddle, K. T. (1985). Deformation and Basin Formation along Strike-Slip
721 Faults1. In K. T. Biddle & N. Christie-Blick (Eds.), *Strike-Slip Deformation, Basin Formation,*
722 *and Sedimentation* (Vol. 37, pp. 0). doi:10.2110/pec.85.37.0001

723 Cunningham, W. D., & Mann, P. (2007). Tectonics of strike-slip restraining and releasing bends.
724 *Geological Society, London, Special Publications*, 290(1), 1. doi:10.1144/SP290.1

725 Dawers, N. H., Anders, M. H., & Scholz, C. H. (1993). Growth of normal faults: Displacement-
726 length scaling. *Geology*, 21(12), 1107. doi:10.1130/0091-7613(1993)021<1107:gonfdl>2.3.co;2

727 de Joussineau, G., & Aydin, A. (2009). Segmentation along Strike-Slip Faults Revisited. 1575-
728 1594. doi:10.1007/978-3-0346-0138-2_3

729 Deng, S., Li, H., Zhang, Z., Zhang, J., & Yang, X. (2019). Structural characterization of
730 intracratonic strike-slip faults in the central Tarim Basin. *AAPG Bulletin*, *103*(1), 109-137.
731 doi:10.1306/06071817354

732 Dooley, T. P., Hudec, M. R., Carruthers, D., Jackson, M. P. A., & Luo, G. (2017). The effects of
733 base-salt relief on salt flow and suprasalt deformation patterns — Part 1: Flow across simple
734 steps in the base of salt. *Interpretation*, *5*(1), SD1-SD23. doi:10.1190/int-2016-0087.1

735 Dooley, T. P., & Schreurs, G. (2012). Analogue modelling of intraplate strike-slip tectonics: A
736 review and new experimental results. *Tectonophysics*, *574-575*, 1-71.
737 doi:10.1016/j.tecto.2012.05.030

738 Dutton, D. M., & Trudgill, B. D. (2009). Four-dimensional analysis of the Sembo relay system,
739 offshore Angola: Implications for fault growth in salt-detached settings. *AAPG Bulletin*, *93*(6),
740 763-794. doi:10.1306/02230908094

741 Duval, B., Cramez, C., & Jackson, M. P. A. (1992). Raft tectonics in the Kwanza Basin, Angola.
742 *Marine and Petroleum Geology*, *9*(4), 389-404. doi:10.1016/0264-8172(92)90050-o

743 Erdi, A., & Jackson, C. A. L. (2021). What controls salt-detached contraction in the translational
744 domain of the outer Kwanza Basin, offshore Angola? *Basin Research*, *33*(3), 1880-1905.
745 doi:10.1111/bre.12539

746 Escalona, A., & Mann, P. (2006). Tectonic controls of the right-lateral Burro Negro tear fault on
747 Paleogene structure and stratigraphy, northeastern Maracaibo Basin. *AAPG Bulletin*, *90*(4), 479-
748 504. doi:10.1306/10070505032

749 Evans, S. L., & Jackson, C. A. L. (2019). Base-salt relief controls salt-related deformation in the
750 Outer Kwanza Basin, offshore Angola. *Basin Research*, *32*(4), 668-687. doi:10.1111/bre.12390

751 Fernandez, N., Duffy, O. B., Peel, F. J., & Hudec, M. R. (2020). Influence of minibasin
752 obstruction on canopy dynamics in the northern Gulf of Mexico. *Basin Research*, *33*(1), 427-
753 446. doi:10.1111/bre.12480

754 Fort, X., & Brun, J.-P. (2012). Kinematics of regional salt flow in the northern Gulf of Mexico.
755 *Geological Society, London, Special Publications*, *363*(1), 265. doi:10.1144/SP363.12

756 Fu, B., & Awata, Y. (2007). Displacement and timing of left-lateral faulting in the Kunlun Fault
757 Zone, northern Tibet, inferred from geologic and geomorphic features. *Journal of Asian Earth*
758 *Sciences*, 29(2), 253-265. doi:<https://doi.org/10.1016/j.jseaes.2006.03.004>

759 Guiraud, M., Buta-Neto, A., & Quesne, D. (2010). Segmentation and differential post-rift uplift
760 at the Angola margin as recorded by the transform-rifted Benguela and oblique-to-orthogonal-
761 rifted Kwanza basins. *Marine and Petroleum Geology*, 27(5), 1040-1068.
762 doi:10.1016/j.marpetgeo.2010.01.017

763 Harding, T. P. (1985). Seismic Characteristics and Identification of Negative Flower Structures,
764 Positive Flower Structures, and Positive Structural Inversion1. *AAPG Bulletin*, 69(4), 582-600.
765 doi:10.1306/AD462538-16F7-11D7-8645000102C1865D

766 Harding, T. P. (1990). Identification of Wrench Faults Using Subsurface Structural Data: Criteria
767 and Pitfalls1. *AAPG Bulletin*, 74(10), 1590-1609. doi:10.1306/0C9B2533-1710-11D7-
768 8645000102C1865D

769 Higgins, S., Clarke, B., Davies, R. J., & Cartwright, J. (2009). Internal geometry and growth
770 history of a thrust-related anticline in a deep water fold belt. *Journal of Structural Geology*,
771 31(12), 1597-1611. doi:<https://doi.org/10.1016/j.jsg.2009.07.006>

772 Hudec, M. R., & Jackson, M. P. A. (2002). Structural segmentation, inversion, and salt tectonics
773 on a passive margin: Evolution of the Inner Kwanza Basin, Angola. *Geological Society of*
774 *America Bulletin*, 114(10), 1222-1244. doi:10.1130/0016-7606(2002)114<1222:ssiast>2.0.co;2

775 Hudec, M. R., & Jackson, M. P. A. (2004). Regional restoration across the Kwanza Basin,
776 Angola: Salt tectonics triggered by repeated uplift of a metastable passive margin. *AAPG*
777 *Bulletin*, 88(7), 971-990. doi:10.1306/02050403061

778 Jachens, R. C., Langenheim, V. E., & Matti, J. C. (2002). Relationship of the 1999 Hector Mine
779 and 1992 Landers Fault Ruptures to Offsets on Neogene Faults and Distribution of Late
780 Cenozoic Basins in the Eastern California Shear Zone. *Bulletin of the Seismological Society of*
781 *America*, 92(4), 1592-1605. doi:10.1785/0120000915

782 Jackson, C. A. L., Bell, R. E., Rotevatn, A., & Tvedt, A. B. M. (2017). Techniques to determine
783 the kinematics of synsedimentary normal faults and implications for fault growth models.
784 *Geological Society, London, Special Publications*, 439(1), 187-217. doi:10.1144/sp439.22

785 Jackson, C. A. L., & Rotevatn, A. (2013). 3D seismic analysis of the structure and evolution of a
786 salt-influenced normal fault zone: A test of competing fault growth models. *Journal of Structural*
787 *Geology*, 54, 215-234. doi:10.1016/j.jsg.2013.06.012

788 Jackson, M. P. A., & Hudec, M. R. (2005). Stratigraphic record of translation down ramps in a
789 passive-margin salt detachment. *Journal of Structural Geology*, 27(5), 889-911.
790 doi:10.1016/j.jsg.2005.01.010

791 Kim, Y.-S., Andrews, J. R., & Sanderson, D. J. (2000). Damage zones around strike-slip fault
792 systems and strike-slip fault evolution, Crackington Haven, southwest England. *Geosciences*
793 *Journal*, 4(2), 53. doi:10.1007/BF02910127

794 Kim, Y.-S., Andrews, J. R., & Sanderson, D. J. (2001). Reactivated strike-slip faults: examples
795 from north Cornwall, UK. *Tectonophysics*, 340(3-4), 173-194. doi:10.1016/s0040-
796 1951(01)00146-9

797 Kim, Y.-S., Peacock, D. C. P., & Sanderson, D. J. (2004). Fault damage zones. *Journal of*
798 *Structural Geology*, 26(3), 503-517. doi:<https://doi.org/10.1016/j.jsg.2003.08.002>

799 Kim, Y.-S., & Sanderson, D. J. (2005). The relationship between displacement and length of
800 faults: a review. *Earth-Science Reviews*, 68(3-4), 317-334. doi:10.1016/j.earscirev.2004.06.003

801 Leduc, A. M., Davies, R. J., Densmore, A. L., & Imber, J. (2012). The lateral strike-slip domain
802 in gravitational detachment delta systems: A case study of the northwestern margin of the Niger
803 Delta. *AAPG Bulletin*, 96(4), 709-728. doi:10.1306/09141111035

804 Lundin, E. R. (1992). Thin-skinned extensional tectonics on a salt detachment, northern Kwanza
805 Basin, Angola. *Marine and Petroleum Geology*, 9(4), 405-411. doi:10.1016/0264-
806 8172(92)90051-f

807 Mann, P. (2007). Global catalogue, classification and tectonic origins of restraining- and
808 releasing bends on active and ancient strike-slip fault systems. *Geological Society, London,*
809 *Special Publications*, 290(1), 13. doi:10.1144/SP290.2

810 Mansfield, C. S., & Cartwright, J. A. (1996). High resolution fault displacement mapping from
811 three-dimensional seismic data: evidence for dip linkage during fault growth. *Journal of*
812 *Structural Geology*, 18(2), 249-263. doi:[https://doi.org/10.1016/S0191-8141\(96\)80048-4](https://doi.org/10.1016/S0191-8141(96)80048-4)

813 Marton, L. G., Tari, G. C., & Lehmann, C. T. (2000). Evolution of the Angolan passive margin,
814 West Africa, with emphasis on post-salt structural styles. *Atlantic Rifts and Continental Margins*,
815 *115*, 129-149. doi:10.1029/GM115p0129

816 Maurin, J.-C., & Guiraud, R. (1993). Basement control in the development of the early
817 cretaceous West and Central African rift system. *Tectonophysics*, *228*(1), 81-95.
818 doi:[https://doi.org/10.1016/0040-1951\(93\)90215-6](https://doi.org/10.1016/0040-1951(93)90215-6)

819 McMillan, R. A. (1975). *The orientation and sense of displacement of strike-slip faults in*
820 *continental crust*. (Bachelor). Carleton University, Ottawa, Ontario.

821 Moulin, M., Aslanian, D., Olivet, J.-L., Contrucci, I., Matias, L., Géli, L., . . . Unternehr, P.
822 (2005). Geological constraints on the evolution of the Angolan margin based on reflection and
823 refraction seismic data (ZaiAngo project). *Geophysical Journal International*, *162*(3), 793-810.
824 doi:10.1111/j.1365-246X.2005.02668.x

825 Nemer, T., & Meghraoui, M. (2006). Evidence of coseismic ruptures along the Roum fault
826 (Lebanon): a possible source for the AD 1837 earthquake. *Journal of Structural Geology*, *28*(8),
827 1483-1495. doi:<https://doi.org/10.1016/j.jsg.2006.03.038>

828 Nicol, A., Childs, C., Walsh, J. J., Manzocchi, T., & Schöpfer, M. P. J. (2017). Interactions and
829 growth of faults in an outcrop-scale system. *Geological Society, London, Special Publications*,
830 *439*(1), 23. doi:10.1144/SP439.9

831 Nicol, A., Watterson, J., Walsh, J. J., & Childs, C. (1996). The shapes, major axis orientations
832 and displacement patterns of fault surfaces. *Journal of Structural Geology*, *18*(2), 235-248.
833 doi:[https://doi.org/10.1016/S0191-8141\(96\)80047-2](https://doi.org/10.1016/S0191-8141(96)80047-2)

834 Nixon, C. W., Sanderson, D. J., & Bull, J. M. (2011). Deformation within a strike-slip fault
835 network at Westward Ho!, Devon U.K.: Domino vs conjugate faulting. *Journal of Structural*
836 *Geology*, *33*(5), 833-843. doi:10.1016/j.jsg.2011.03.009

837 Omosanya, K. O., Zervas, I., Mattos, N. H., Alves, T. M., Johansen, S. E., & Marfo, G. (2017).
838 Strike-Slip Tectonics in the SW Barents Sea During North Atlantic Rifting (Swaen Graben,
839 Northern Norway). *Tectonics*, *36*(11), 2422-2446. doi:10.1002/2017TC004635

840 Pan, S., Bell, R. E., Jackson, C. A. L., & Naliboff, J. (2022). Evolution of normal fault
841 displacement and length as continental lithosphere stretches. *Basin Research*, 34(1), 121-140.
842 doi:<https://doi.org/10.1111/bre.12613>

843 Peacock, D. C. P. (1991). Displacements and segment linkage in strike-slip fault zones. *Journal*
844 *of Structural Geology*, 13(9), 1025-1035. doi:10.1016/0191-8141(91)90054-m

845 Peacock, D. C. P., & Sanderson, D. J. (1994). Geometry and Development of Relay Ramps in
846 Normal Fault Systems. *AAPG Bulletin*, 78(2), 147-165. doi:10.1306/BDF9046-1718-11D7-
847 8645000102C1865D

848 Peacock, D. C. P., & Sanderson, D. J. (1995). Strike-slip relay ramps. *Journal of Structural*
849 *Geology*, 17(10), 1351-1360. doi:10.1016/0191-8141(95)97303-w

850 Pichel, L. M., Jackson, C. A. L., Peel, F., & Dooley, T. P. (2019). Base-salt relief controls salt-
851 tectonic structural style, São Paulo Plateau, Santos Basin, Brazil. *Basin Research*, 32(3), 453-
852 484. doi:10.1111/bre.12375

853 Reeve, M. T., Bell, R. E., Duffy, O. B., Jackson, C. A. L., & Sansom, E. (2015). The growth of
854 non-colinear normal fault systems; What can we learn from 3D seismic reflection data? *Journal*
855 *of Structural Geology*, 70, 141-155. doi:10.1016/j.jsg.2014.11.007

856 Rotevatn, A., Jackson, C. A. L., Tvedt, A. B. M., Bell, R. E., & Blækkan, I. (2019). How do
857 normal faults grow? *Journal of Structural Geology*, 125, 174-184.
858 doi:<https://doi.org/10.1016/j.jsg.2018.08.005>

859 Rovida, A., & Tibaldi, A. (2005). Propagation of strike-slip faults across Holocene volcano-
860 sedimentary deposits, Pasto, Colombia. *Journal of Structural Geology*, 27(10), 1838-1855.
861 doi:<https://doi.org/10.1016/j.jsg.2005.06.009>

862 Rowan, M. G., Hart, B. S., Nelson, S., Flemings, P. B., & Trudgill, B. D. (1998). Three-
863 dimensional geometry and evolution of a salt-related growth-fault array: Eugene Island 330 field,
864 offshore Louisiana, Gulf of Mexico. *Marine and Petroleum Geology*, 15(4), 309-328.
865 doi:10.1016/s0264-8172(98)00021-x

866 Rowan, M. G., Jackson, M. P. A., & Trudgill, B. D. (1999). Salt-Related Fault Families and
867 Fault Welds in the Northern Gulf of Mexico. *AAPG Bulletin*, 83(9), 1454-1484.
868 doi:10.1306/e4fd41e3-1732-11d7-8645000102c1865d

869 Scholz, C. H., & Cowie, P. A. (1990). Determination of total strain from faulting using slip
870 measurements. *Nature*, 346(6287), 837-839. doi:10.1038/346837a0

871 Sieh, K., & Natawidjaja, D. (2000). Neotectonics of the Sumatran fault, Indonesia. *Journal of*
872 *Geophysical Research: Solid Earth*, 105(B12), 28295-28326.
873 doi:<https://doi.org/10.1029/2000JB900120>

874 Sylvester, A. G. (1988). Strike-slip faults. *GSA Bulletin*, 100(11), 1666-1703. doi:10.1130/0016-
875 7606(1988)100<1666:SSF>2.3.CO;2

876 Tatar, O., Piper, J. D. A., Gürsoy, H., Heimann, A., & Koçbulut, F. (2004). Neotectonic
877 deformation in the transition zone between the Dead Sea Transform and the East Anatolian Fault
878 Zone, Southern Turkey: a palaeomagnetic study of the Karasu Rift Volcanism. *Tectonophysics*,
879 385(1), 17-43. doi:<https://doi.org/10.1016/j.tecto.2004.04.005>

880 Thorsen, C. E. (1963). Age of growth faulting in south-east Louisiana. *Gulf Coasts Association of*
881 *Geologists Societies Transactions*, 13, 103-110.

882 Torabi, A., & Berg, S. S. (2011). Scaling of fault attributes: A review. *Marine and Petroleum*
883 *Geology*, 28(8), 1444-1460. doi:10.1016/j.marpetgeo.2011.04.003

884 Tvedt, A. B. M., Rotevatn, A., & Jackson, C. A. L. (2016). Supra-salt normal fault growth during
885 the rise and fall of a diapir: Perspectives from 3D seismic reflection data, Norwegian North Sea.
886 *Journal of Structural Geology*, 91, 1-26. doi:10.1016/j.jsg.2016.08.001

887 Von Nicolai, C. (2011). *The Interplay of Salt Movements and Regional Tectonics at the Passive*
888 *Continental Margin of the South Atlantic, Kwanza Basin*. (PhD thesis). Universität Potsdam,
889 Retrieved from [<https://goo.gl/8LwQBY>]

890 Wagner, B. H., & Jackson, M. P. A. (2011). Viscous flow during salt welding. *Tectonophysics*,
891 510(3-4), 309-326. doi:10.1016/j.tecto.2011.07.012

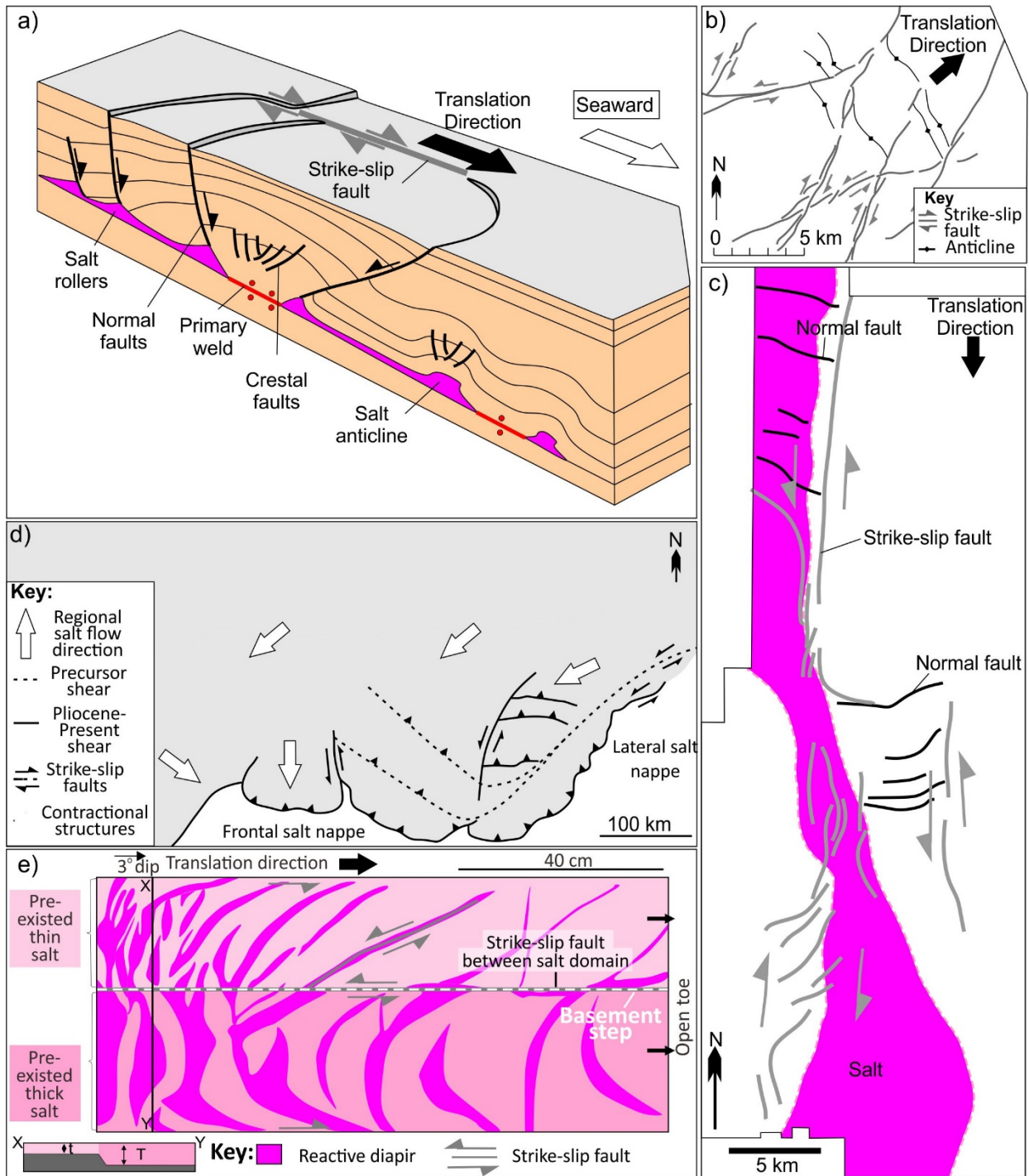
- 892 Walker, R., & Jackson, J. (2002). Offset and evolution of the Gowk fault, S.E. Iran: a major
893 intra-continental strike-slip system. *Journal of Structural Geology*, 24(11), 1677-1698.
894 doi:[https://doi.org/10.1016/S0191-8141\(01\)00170-5](https://doi.org/10.1016/S0191-8141(01)00170-5)
- 895 Walsh, J. J., Nicol, A., & Childs, C. (2002). An alternative model for the growth of faults.
896 *Journal of Structural Geology*, 24(11), 1669-1675. doi:[https://doi.org/10.1016/S0191-](https://doi.org/10.1016/S0191-8141(01)00165-1)
897 [8141\(01\)00165-1](https://doi.org/10.1016/S0191-8141(01)00165-1)
- 898 Walsh, J. J., & Watterson, J. (1988). Analysis of the relationship between displacements and
899 dimensions of faults. *Journal of Structural Geology*, 10(3), 239-247.
900 doi:[https://doi.org/10.1016/0191-8141\(88\)90057-0](https://doi.org/10.1016/0191-8141(88)90057-0)
- 901 Walsh, J. J., & Watterson, J. (1989). Displacement gradients on fault surfaces. *Journal of*
902 *Structural Geology*, 11(3), 307-316. doi:[https://doi.org/10.1016/0191-8141\(89\)90070-9](https://doi.org/10.1016/0191-8141(89)90070-9)
- 903 Wesnousky, S. G. (1988). Seismological and structural evolution of strike-slip faults. *Nature*,
904 335(6188), 340-343. doi:10.1038/335340a0

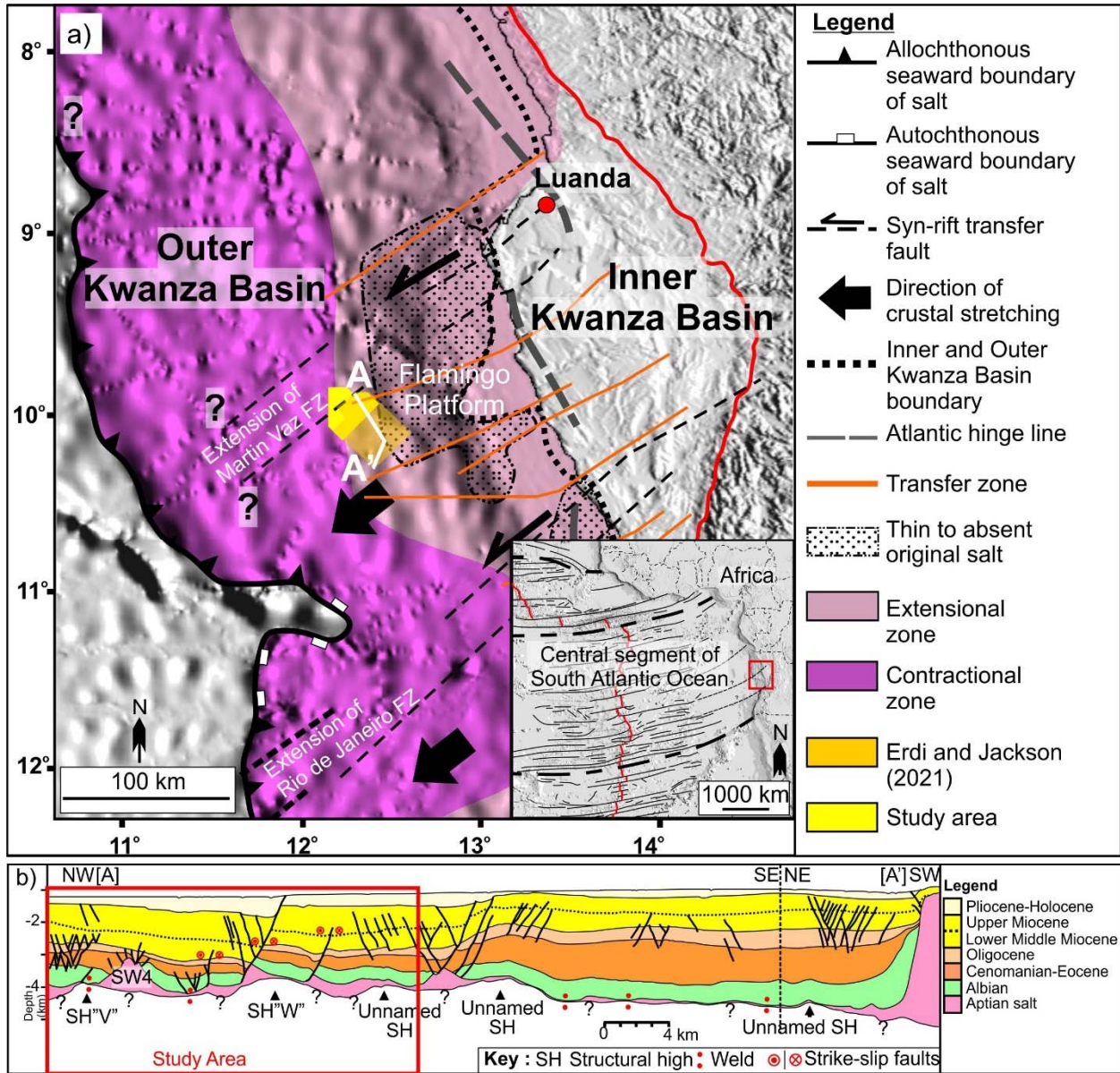
905 **Table**

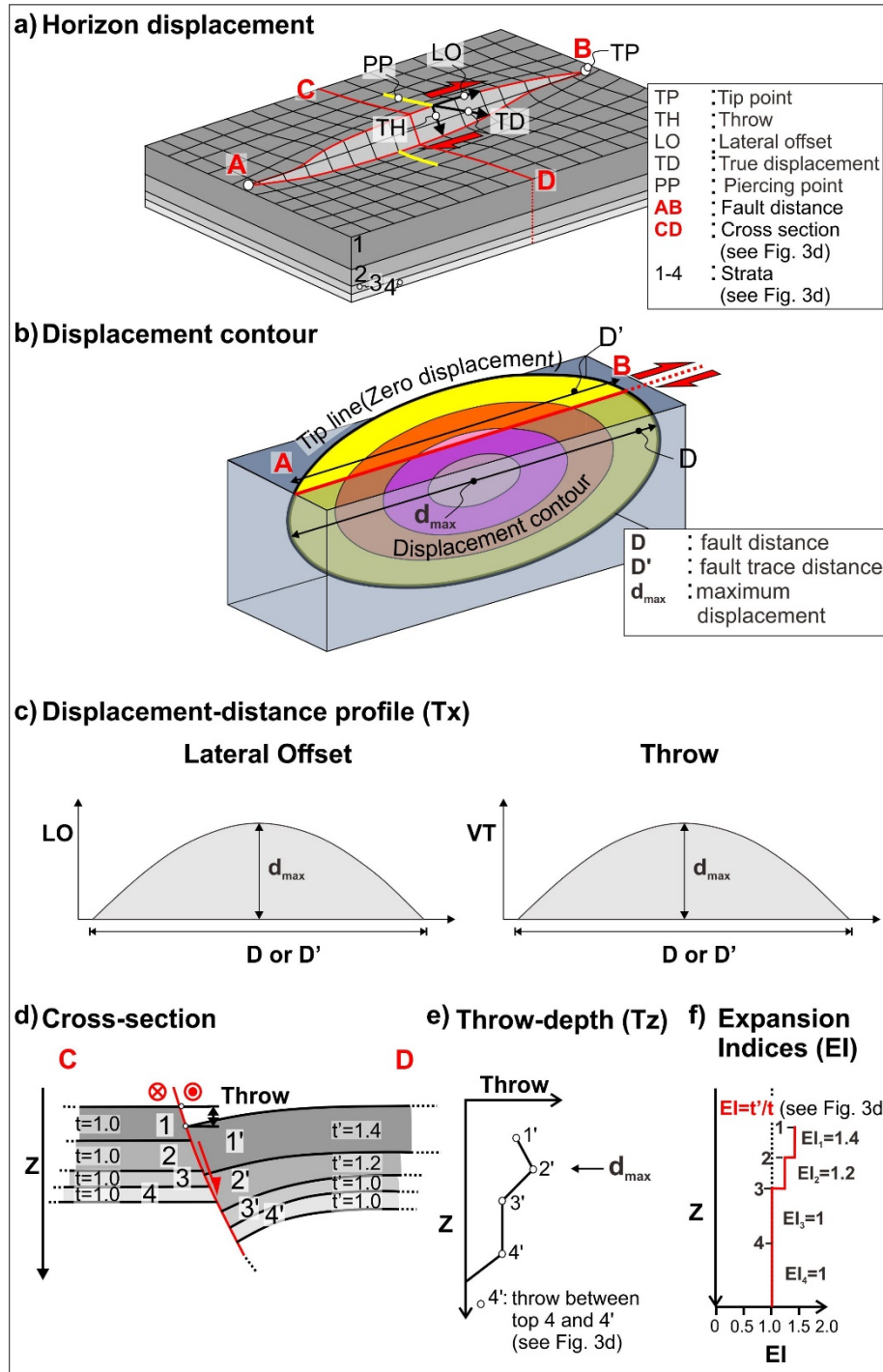
906 Table 1

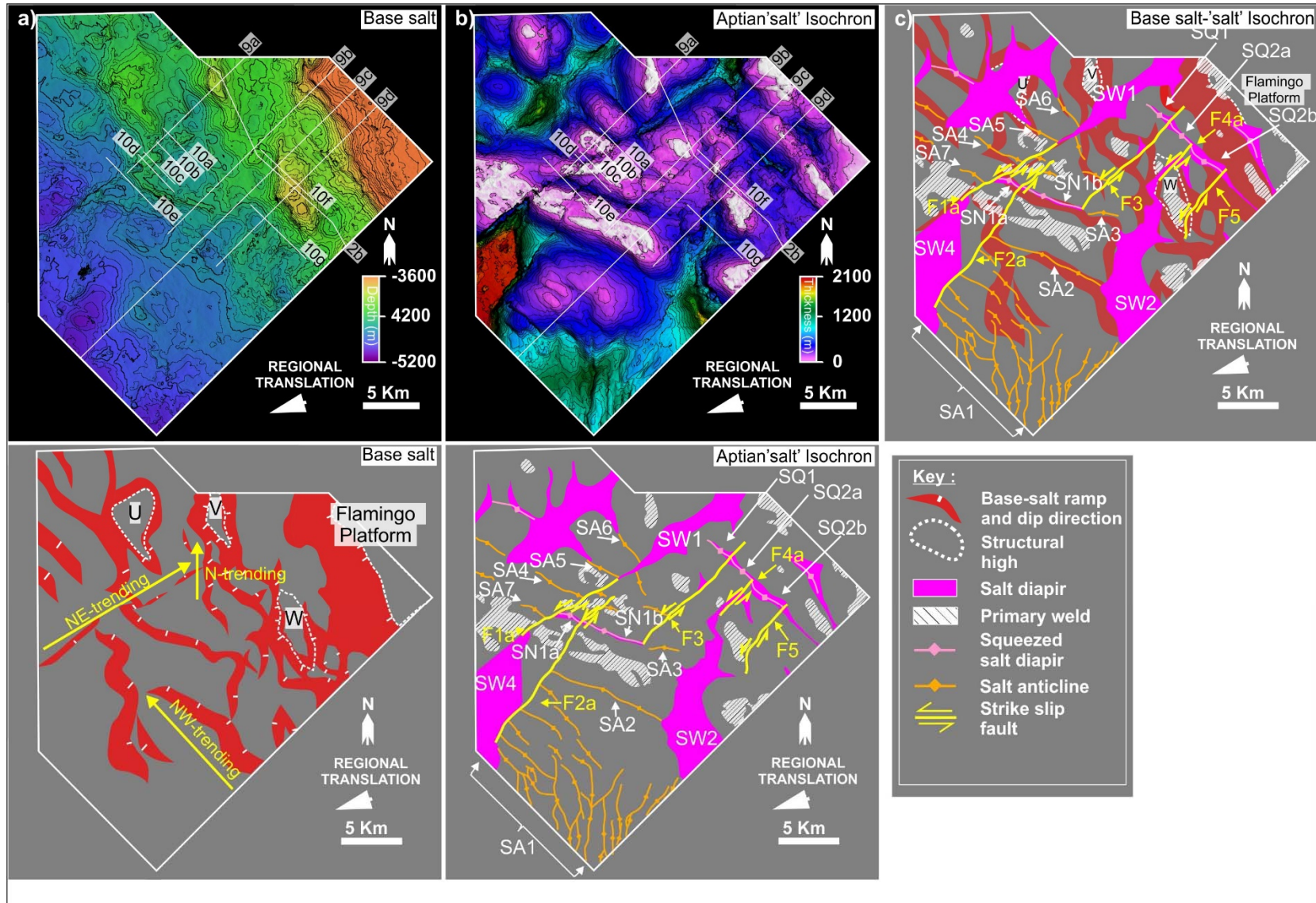
Structural level	Sub-domain	Description of deformation and stratigraphic features
Albian and Eocene	1	A strongly deformed domain, characterised by: <ul style="list-style-type: none"> ▪ Four NW-trending salt anticlines (SA4-7) ▪ Two NW-trending salt-detached thrust faults ▪ Up to 17, N- or NE-trending, salt-detached normal faults
	2	A weakly deformed domain, characterised by: <ul style="list-style-type: none"> ▪ a NW-trending salt anticline and squeezed diapir (SN1a) ▪ Up to 11, N-trending, salt-detached normal faults
	3	A high degree deformation domain, being reflected by: <ul style="list-style-type: none"> ▪ Up to 13, NW-, N- or NE-trending, salt anticlines (SA1) ▪ Up to 49, NW- or NE-trending, salt-detached normal fault
	4	A moderately deformed domain, characterised by: <ul style="list-style-type: none"> ▪ Five NW- or N-trending salt anticlines and a squeezed diapir (SN1b and SQ1) ▪ Up to 20, N- or NE-trending, salt-detached normal faults
	5	A weakly deformed domain, characterised by: <ul style="list-style-type: none"> ▪ Two NW- or W-trending, salt anticline (SA3) and squeezed diapir (SQ2a) ▪ Up to 10, NW- or N-trending, salt-detached normal faults
	6	A weakly deformed domain, characterised by: <ul style="list-style-type: none"> ▪ a NW-trending squeezed diapir (SQ2b) ▪ Up to 4, NW-trending, salt-detached normal faults
Upper Miocene	1	A weakly deformed domain, characterised by: <ul style="list-style-type: none"> ▪ Three NW-trending salt-detached normal faults ▪ A NW-trending channel
	2	A weakly deformed domain, characterised by: <ul style="list-style-type: none"> ▪ Up to 17, NW-trending, salt-detached normal faults ▪ Five W-, NW-, or N-trending channels
	3	
	4	
	5	A largely undeformed domain, characterized by: <ul style="list-style-type: none"> ▪ A W-trending channel
	6	

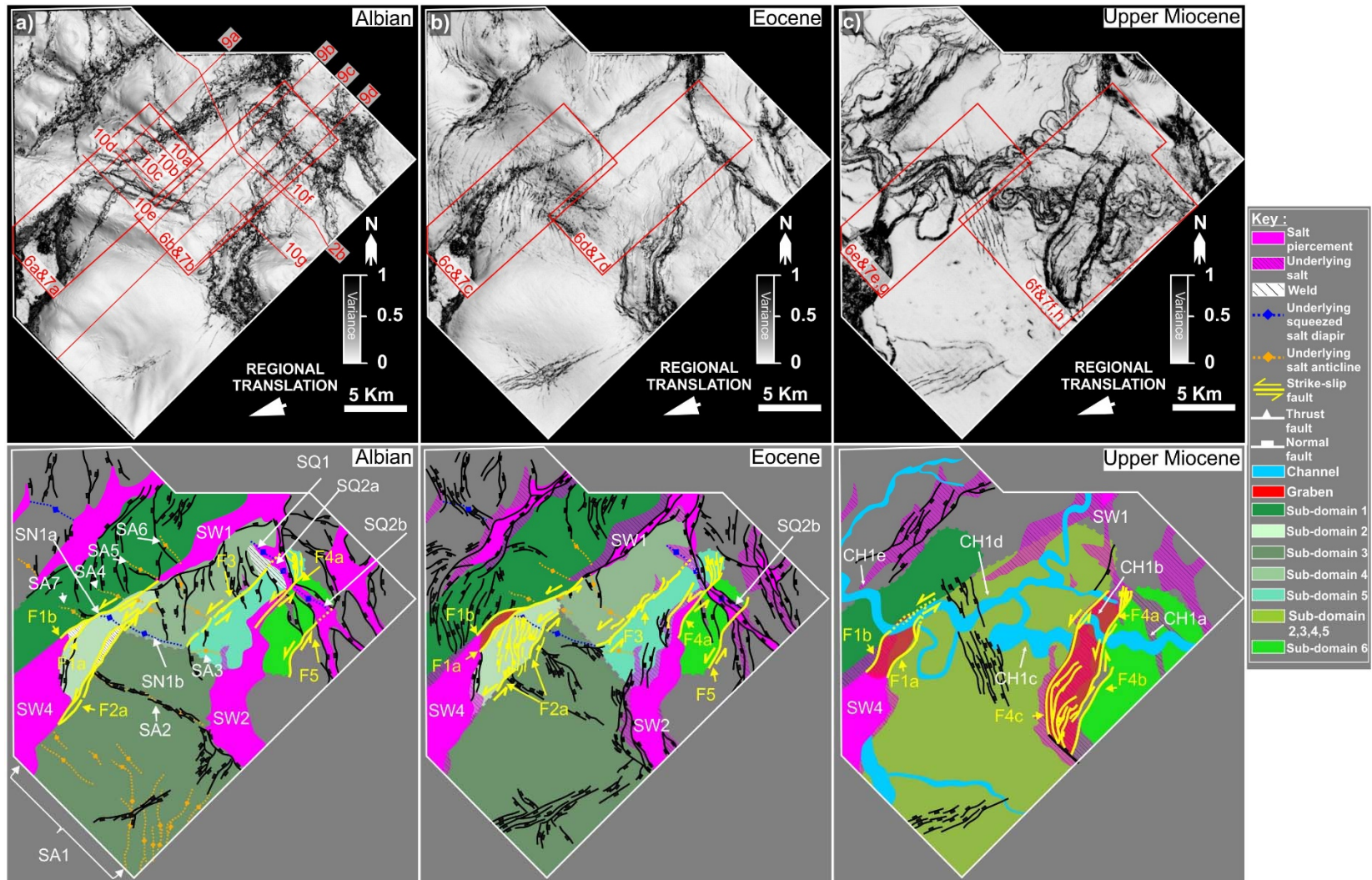
907

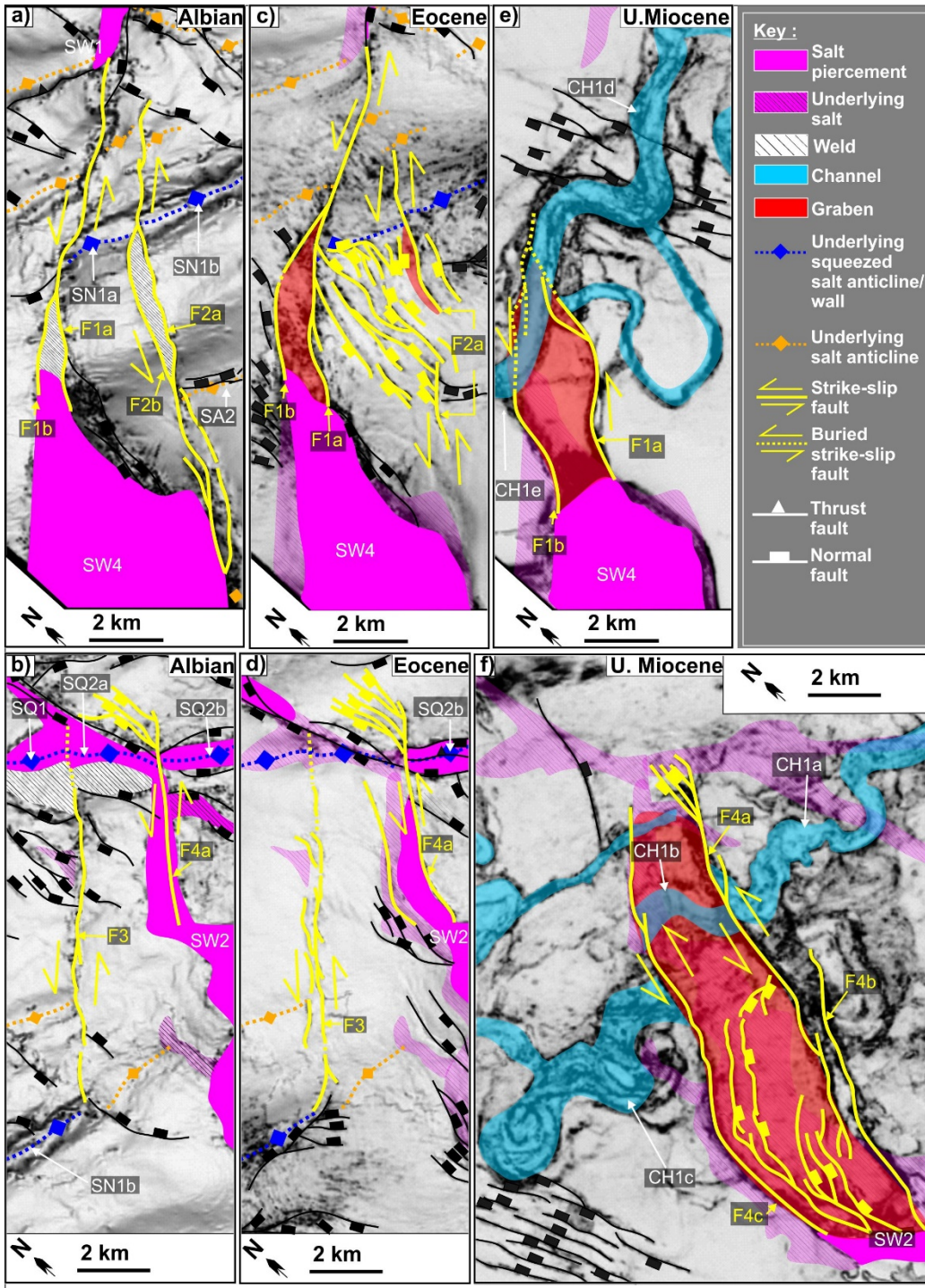












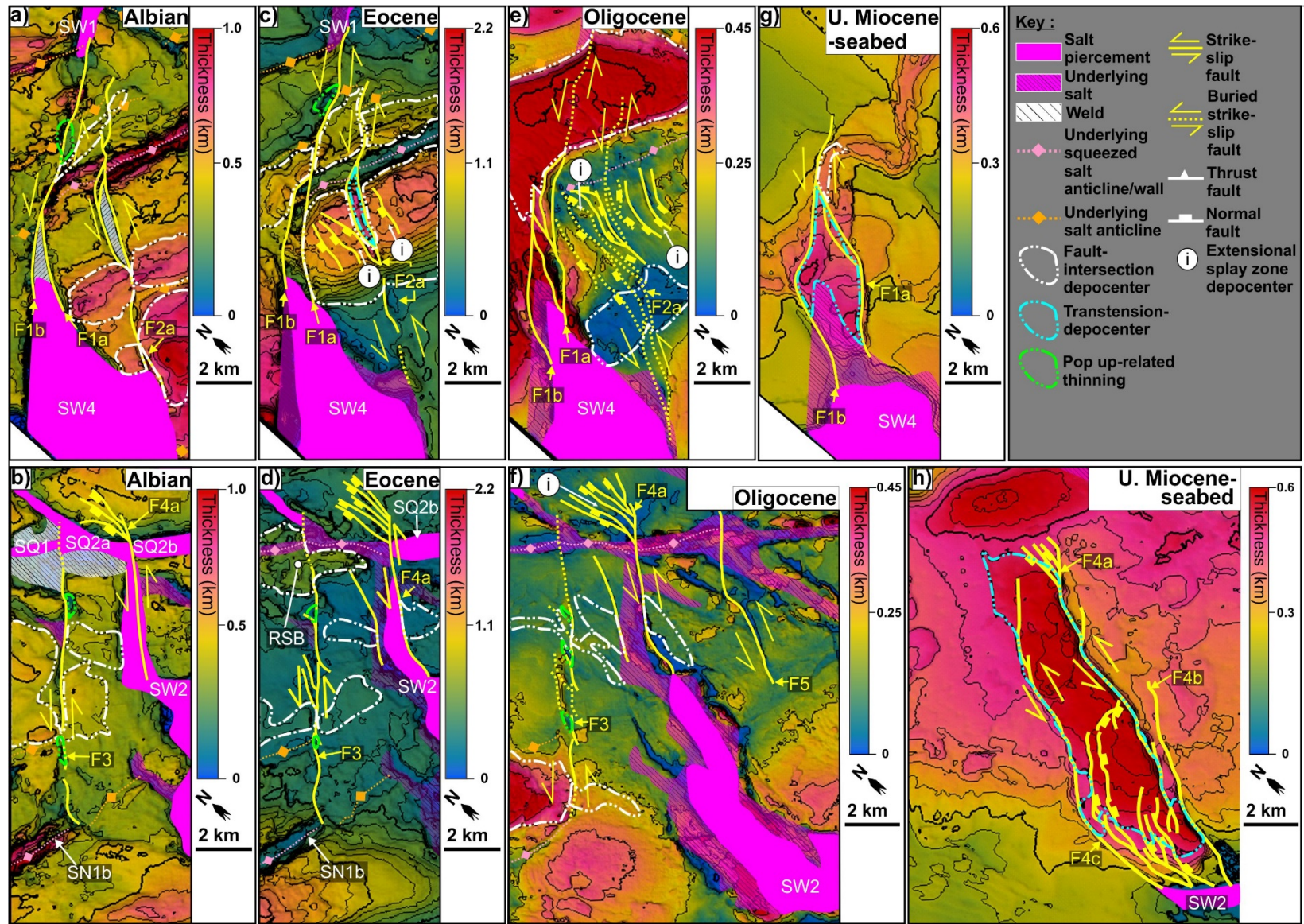
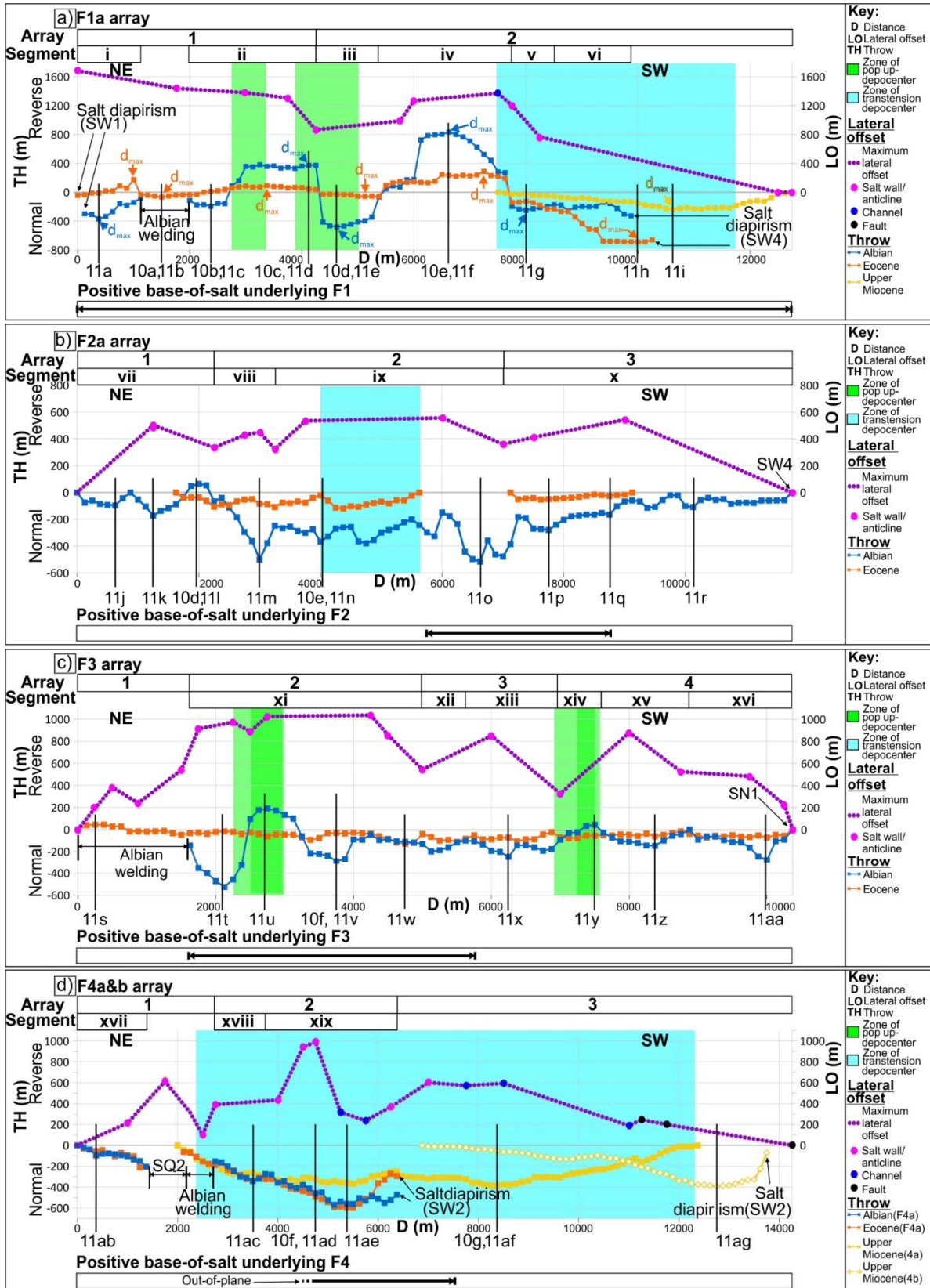
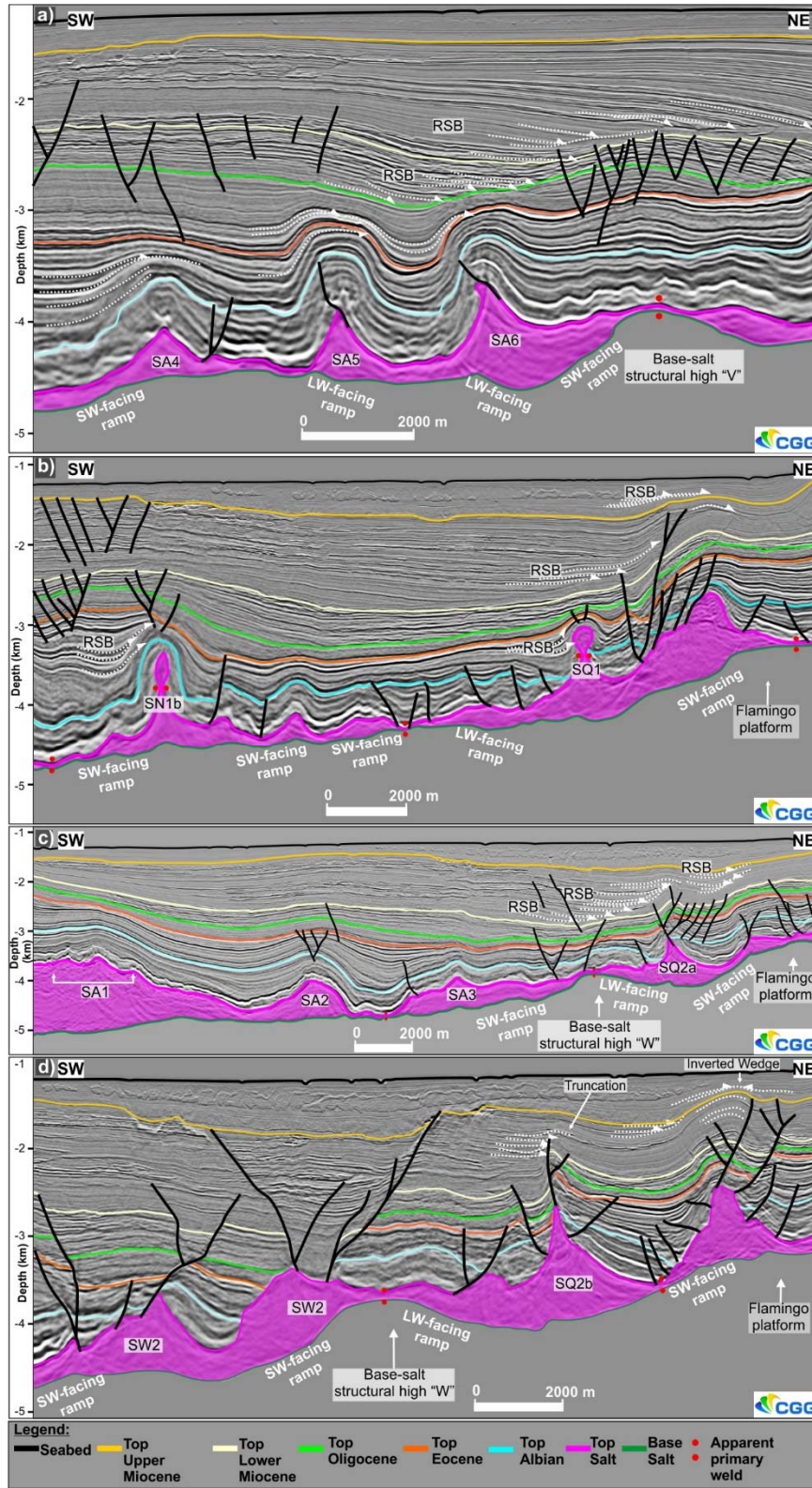
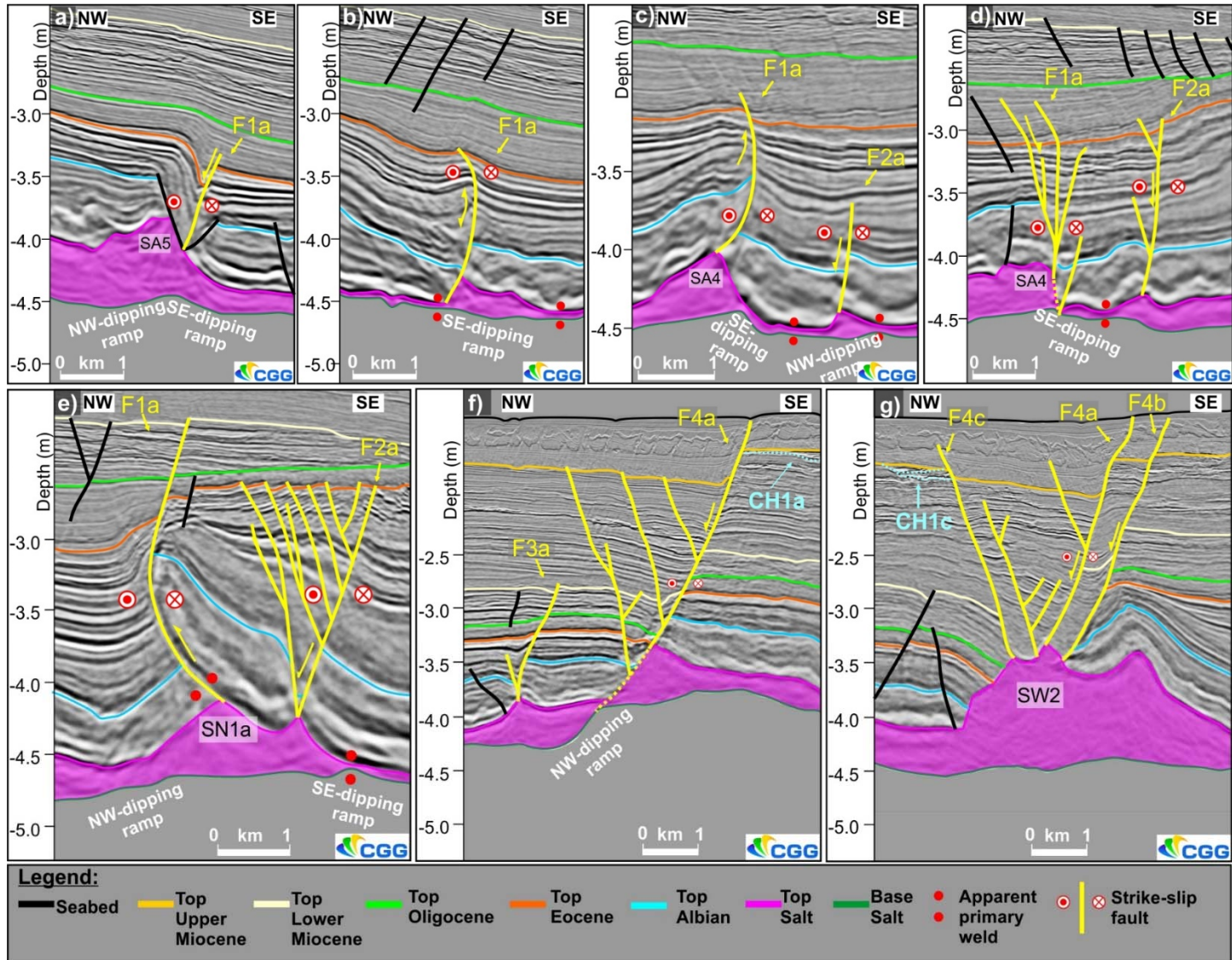
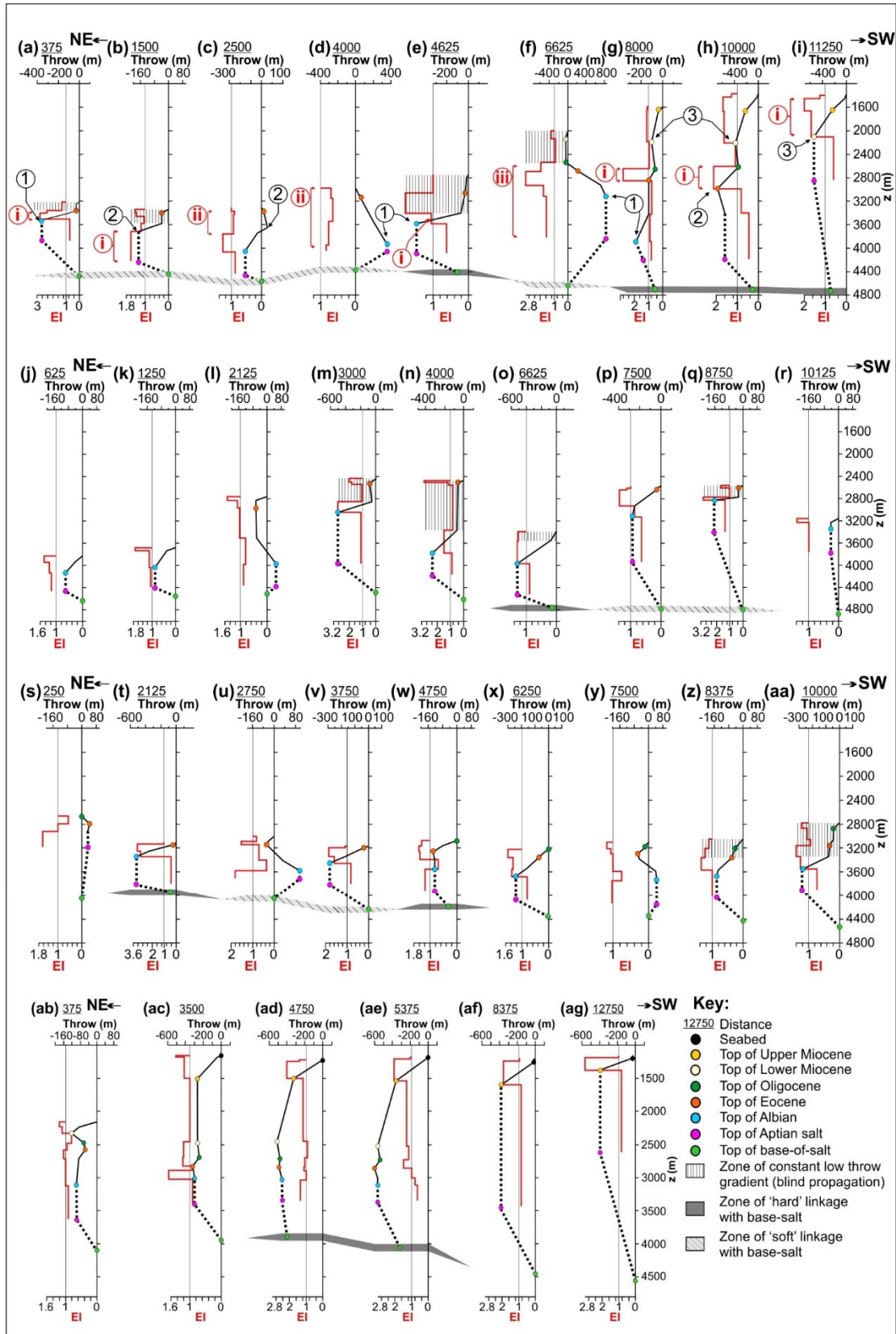


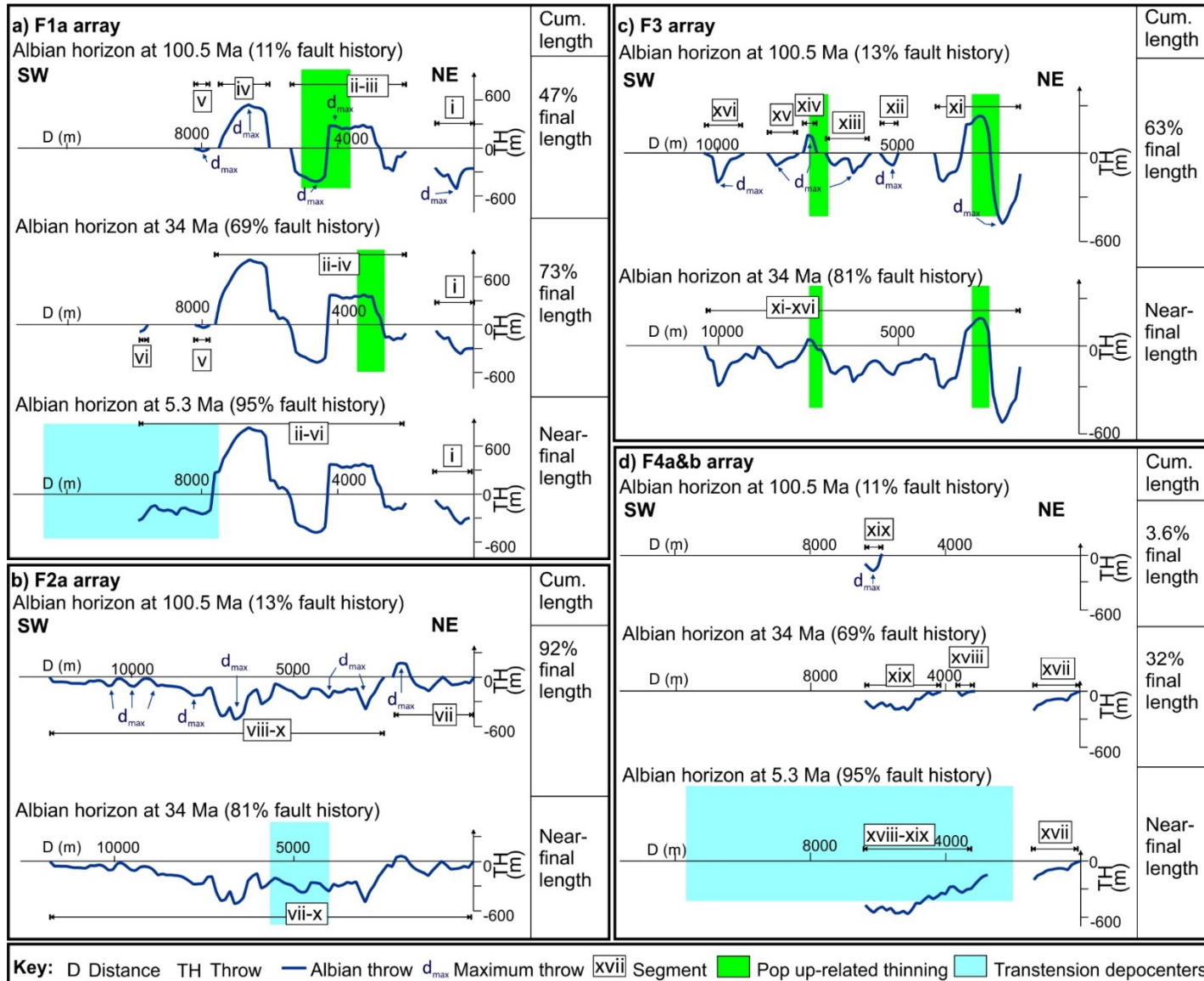
Figure 8

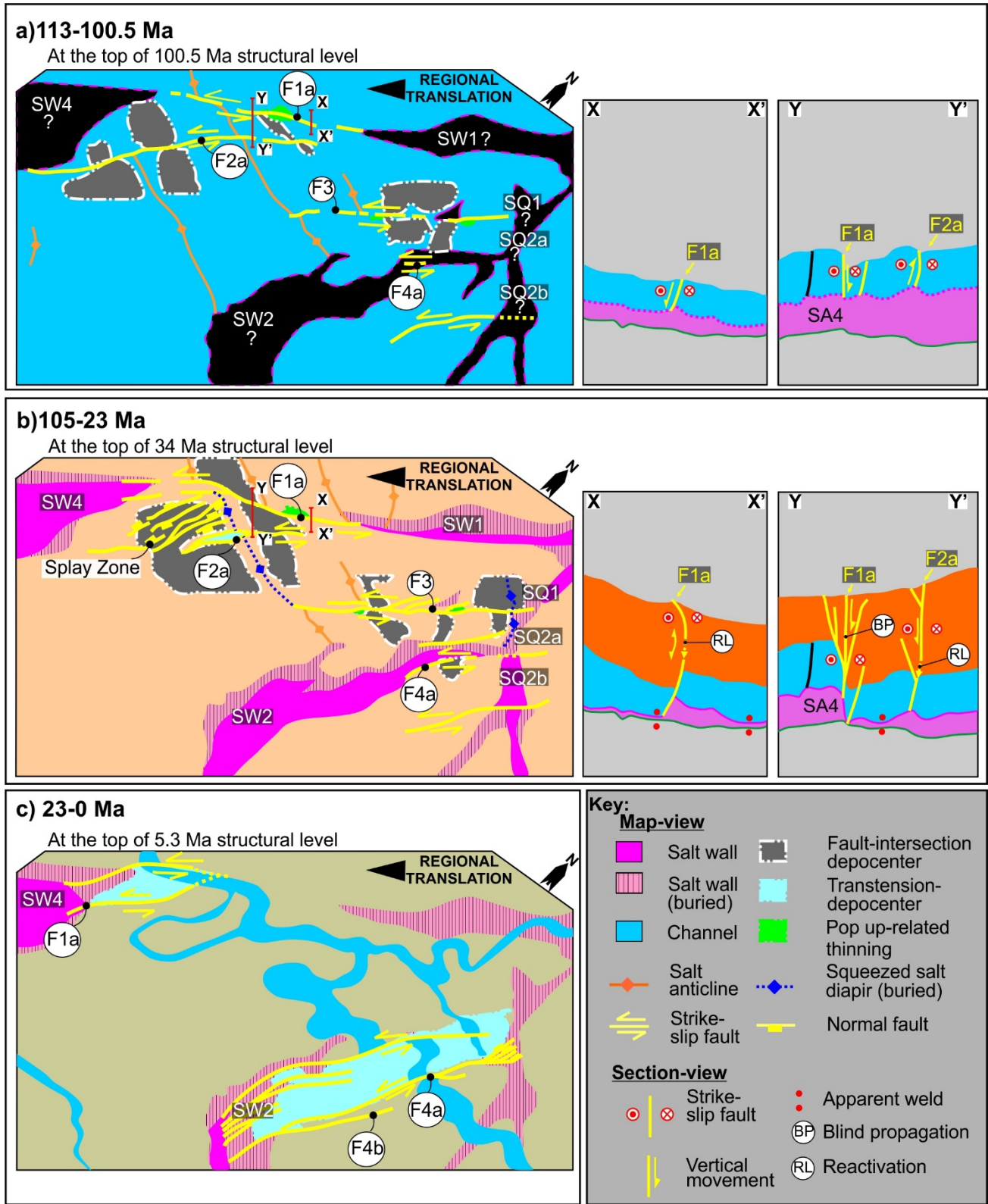


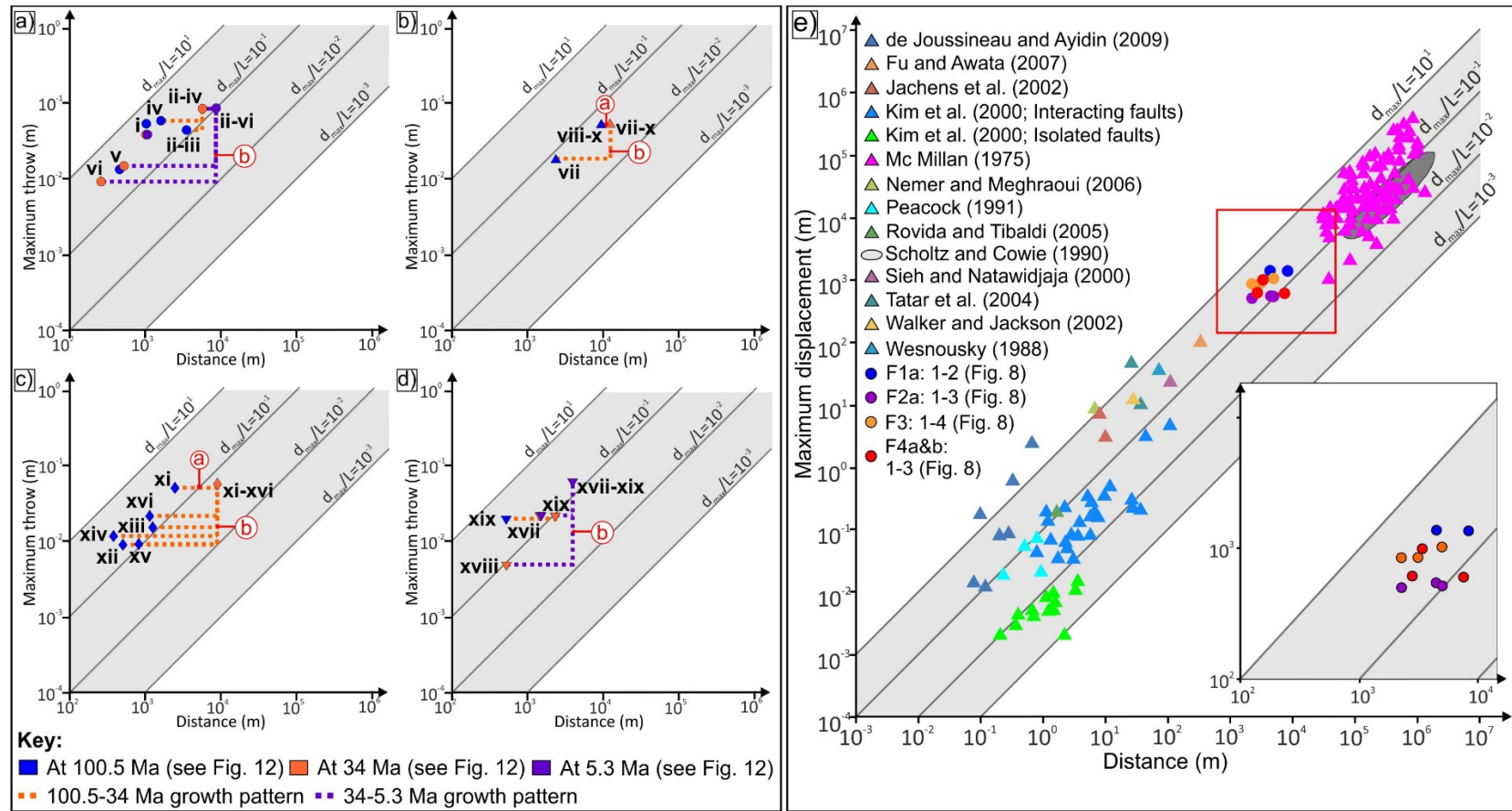












937

Supporting Information for

938

Salt-detached strike-slip faulting, Outer Kwanza Basin, Offshore Angola

939

Aurio Erdi^{1,2}, Christopher A-L. Jackson^{1,†}

940

941

¹Basin Research Group (BRG), Department of Earth Science and Engineering, Imperial

942

College, Prince Consort Road, London, SW7 2BP, UK, ²National Research and Innovation

943

Agency (BRIN), Indonesia, [†] Basin Studies Group, Department of Earth, Atmospheric and

944

Environmental Sciences, University of Manchester, Oxford Road, Manchester, M13 9PL, UK

945

946

Contents of this file

947

Appendix A. Methodology of Fault Geometry and Kinematics

948

A1. Displacement-distance analysis (Tx)

949

A2. Backstripping

950

A3. Fault growth trajectory

951

A4. Throw-depth (Tz)

952

A5. Expansion indice (EI)

953

A6. Isopach map

954

Figures S1. Similar figure with Figure 3 in the main text, illustrating nomenclature and

955

technique to determine geometry of strike-slip faults in this study. (a) oblique view of

956

strike-slip fault; (b) displacement contour on the fault surface; (c) lateral offset and

957

vertical separation displacement profile; (d) hypothetical two-dimensional cross section

958

of a master strike-slip fault; (e) vertical separation-depth; (f) Expansion indices

959

Appendix B. Uninterpreted seismic cross-sections

960

Figures S2. Uninterpreted cross sections of Figure 9 that are perpendicular to basin

961

margin and across different domains that are separated by strike-slip faults (section

962

locations shown in Figures 4a-b and 5a in the main text). Seismic data courtesy of CGG

963

Earth data (previously CGG Multi-Client).

964 Figures S3. Uninterpreted cross sections of Figure 10 across strike-slip faults in the
965 study area (section locations shown in Figures 4a-b and 5a in the main text). Seismic
966 data courtesy of CGG Earth data (previously CGG Multi-Client).

967 Appendix C. Uninterpreted and interpretative sketch of variance and isopach maps

968 Figures S4. Uninterpreted zoom in variance map (Figure 6 in main text) at (a-b) Albian,
969 (c-d) Eocene and (e-f) Upper Miocene structural level, documenting variation of map-
970 view geometry of strike-slip faults (map locations shown in Figure 5). Seismic data
971 courtesy of CGG Earth data (previously CGG Multi-Client).

972 Figure S5. Interpretative sketch map (Figure 6 in main text) of zoom in variance map
973 (Figure S4).

974 Figure S6. Uninterpreted isopach maps (Figure 7 in main text) of (a-b) Aptian-Albian,
975 (c-d) Albian-Eocene, (e-f) Eocene-Oligocene, (g-h) Upper Miocene to seabed.

976 Figure S7. Interpretative sketch (Figure 6 in main text) for isopach maps (Figure S6) of
977 (a-b) Aptian-Albian, (c-d) Albian-Eocene, (e-f) Eocene-Oligocene, (g-h) Upper
978 Miocene to seabed.

979 Appendix D. Data measurements of salt-detached strike-slip faults and collections of global
980 datasets of strike-slip faults

981 Table S1. Lateral Offset-distance

982 Table S2. Throw-distance (Tx)

983 Table S3. Global and our dataset of strike-slip faults

984 References

985 **Introduction**

986 This supporting information provides: (i) methodological description of fault geometry and
987 kinematic (chapter 3 in main text), (ii) Uninterpreted seismic cross section, (iii) uninterpreted
988 and interpretative sketch of variance and isopach maps, (iv) data measurement of throw and
989 lateral offset of strike-slip fault arrays in the Outer Kwanza Basin (Figure 8 in main text) and
990 collection of global datasets of strike-slip faults (Figures 14c main text).

991 **Appendix A. Methodology of Fault Geometry and Kinematics**

992 We use five techniques to document three-dimensional geometry of and investigate
993 temporal and spatial evolution of salt-detached strike-slip faults above base-salt reliefs,
994 including: i) displacement-distance analysis (Tx); ii) backstripping; iii) fault growth trajectory;
995 iv) vertical separation-depth (c.f. Tz); v) expansion indice (EI); and, vi) isopach map (Fig. S1).

996 **A1. Displacement-distance analysis (Tx)**

997 We conduct displacement-distance analysis (Tx), focusing on the lateral offset of piercing
998 points (i.e. pre-faulting salt structures, channels) (e.g. Peacock, 1991; Kim et al., 2001; 2003;
999 Nixon et al., 2011) *and* the throw of key (seismic) stratigraphic marker horizons (Omosanya et
1000 al., 2017; Deng et al., 2019) (Fig. S1a-c). Whereas the density of measurements to constrain
1001 lateral offset is dependent on the number of piercing points, the vertical separation is
1002 systematically recorded by measuring horizon separation on regularly spaced (125 m) sections
1003 oriented perpendicular to the local strike of either master faults or the underlying base-salt relief
1004 (see Deng et al., 2019; see also Jackson et al., 2017). We used the throw patterns revealed by
1005 our analysis of lateral offset and throw, in particular the presence of strain minima, to detect
1006 the positions of linkage between fault segments (e.g. Jackson and Rotevatn, 2013; Tvedt et al.,
1007 2016).

1008 **A2. Backstripping**

1009 We backstrip the throw data to constrain fault kinematics, following similar approach in
1010 normal faults (e.g. Jackson et al., 2017). In our study, this method reveals growth in throw
1011 accumulation and length of strike-slip faults at times. There are two different backstripping
1012 techniques, comprising of: (i) maximum throw subtraction method (Rowan et al., 1998; Dutton
1013 and Trudgill, 2009), which honour increasing of fault length as displacement accumulates (e.g.
1014 Walsh and Watterson 1988); and, (ii) vertical throw subtraction method (Chapman and
1015 Meneilly, 1991; Petersen et al., 1992), which use for a typical fault that has established a near-

1016 constant fault length rapidly from an early stage (e.g. Tvedt et al., 2016; Pan et al., 2020). We
1017 account for two different reasons that collectively point to the “maximum throw subtraction
1018 method’ as a suitable technique for strike-slip faults in the Outer Kwanza Basin. The first
1019 reason is that the maximum throw subtraction method, through fault kinematic, promotes fault
1020 segments linkage (see Dutton and Trudgill, 2009), a typical geometry and kinematic of strike-
1021 slip faults (e.g. Kim and Sanderson, 2005). The second reason is that thickness changes and
1022 sediment accumulations across the strike-slip faults and base-salt reliefs do not influence
1023 general throw (i.e. vertical component of displacement) distribution; thus, the thickness
1024 changed and pre-faulting stratigraphic architecture, as erroneous problems of the maximum
1025 throw method, that may influence fault kinematics can be neglected (Jackson, et al., 2017).

1026 **A3. Fault growth trajectory**

1027 We construct fault growth trajectory using changes in the throw-distance relationships at
1028 Albian structural level derived from backstripping (cf. Pan et al., 2022). We choose to only use
1029 the Albian structural level due this stratum reflects pre-kinematic stage in Outer Kwanza (Erdi
1030 and Jackson, 2021); thus, this stratum records cumulative strain from early- to late- kinematic
1031 stages.

1032 **A4. Throw-depth (Tz)**

1033 We use throw-depth analysis (c.f. T-z) to assess the role of dip linkage in fault growth (Fig.
1034 S1d) (e.g. Mansfield and Cartwright, 1995; Cartwright et al., 1998; Tvedt et al., 2016; Jackson
1035 and Rotevatn, 2013). The T-z plots were constructed at the location of maximum vertical
1036 separation of the Albian and Upper Miocene horizons, whether normal or reverse, on individual
1037 segments. Note that, due to seismically imaged of intrasalt stratigraphic horizons, we cannot
1038 determine the vertical separation at top salt; we instead assign the nearest separation values of
1039 strike-slip faults at the overlying overburden to define them.

1040 **A5. Expansion indice (EI)**

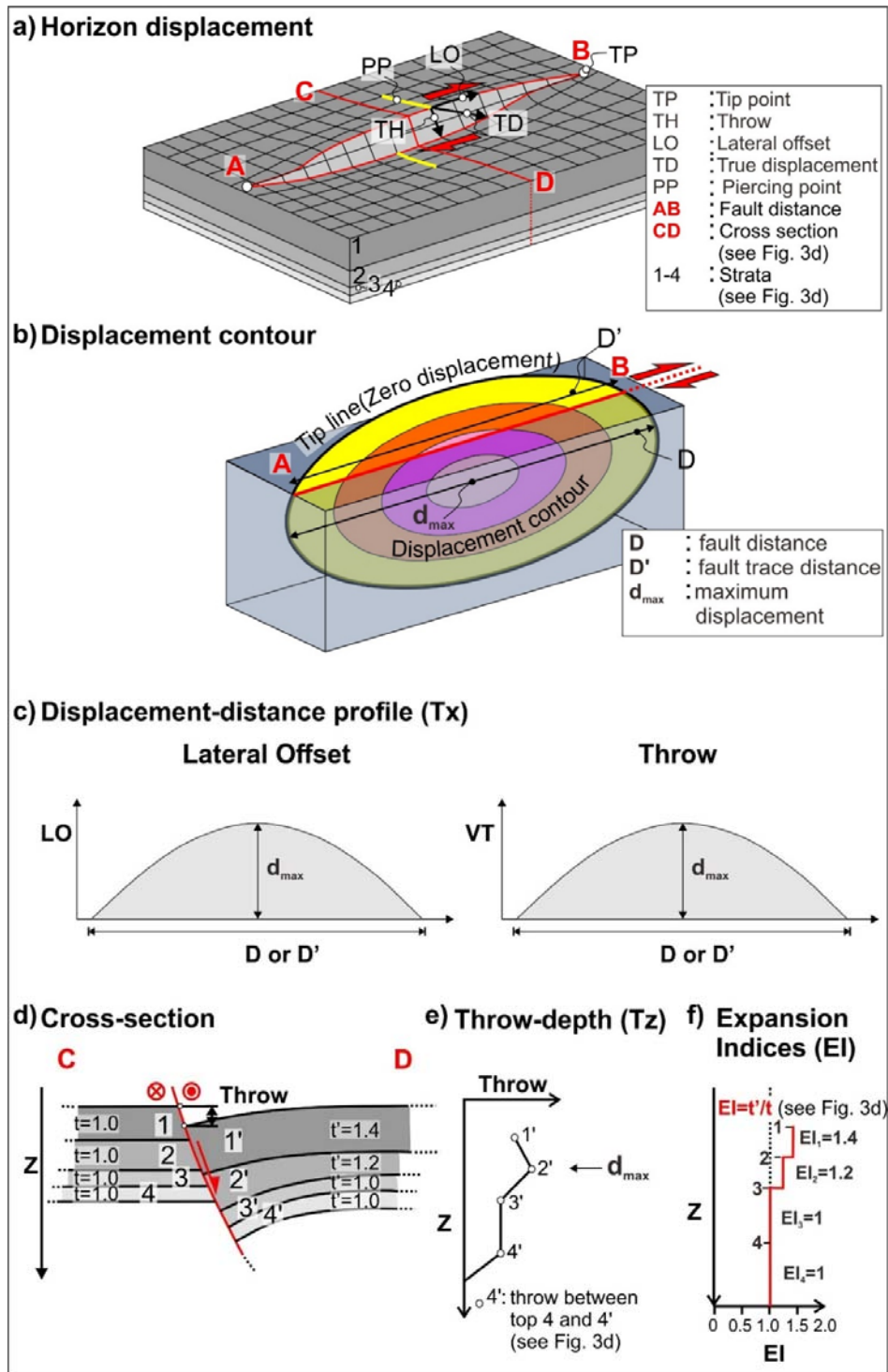
1041 We construct expansion indices (EI) to investigate thickness variation of growth strata,
1042 which reveal temporal activity of the fault kinematics (Fig. S1f) (e.g. Thorsen, 1963; Jackson
1043 and Rotevatn, 2013; Reeve et al., 2015; Tvedt et al., 2016).

1044 **A6. Isopach map**

1045 We make isopach maps to track changes in subsidence and accommodation that mainly
1046 relate to the growth of the strike-slip fault array and adjacent salt structures (e.g. Jackson and
1047 Rotevatn, 2013; Tvedt et al, 2013).

1048

1049



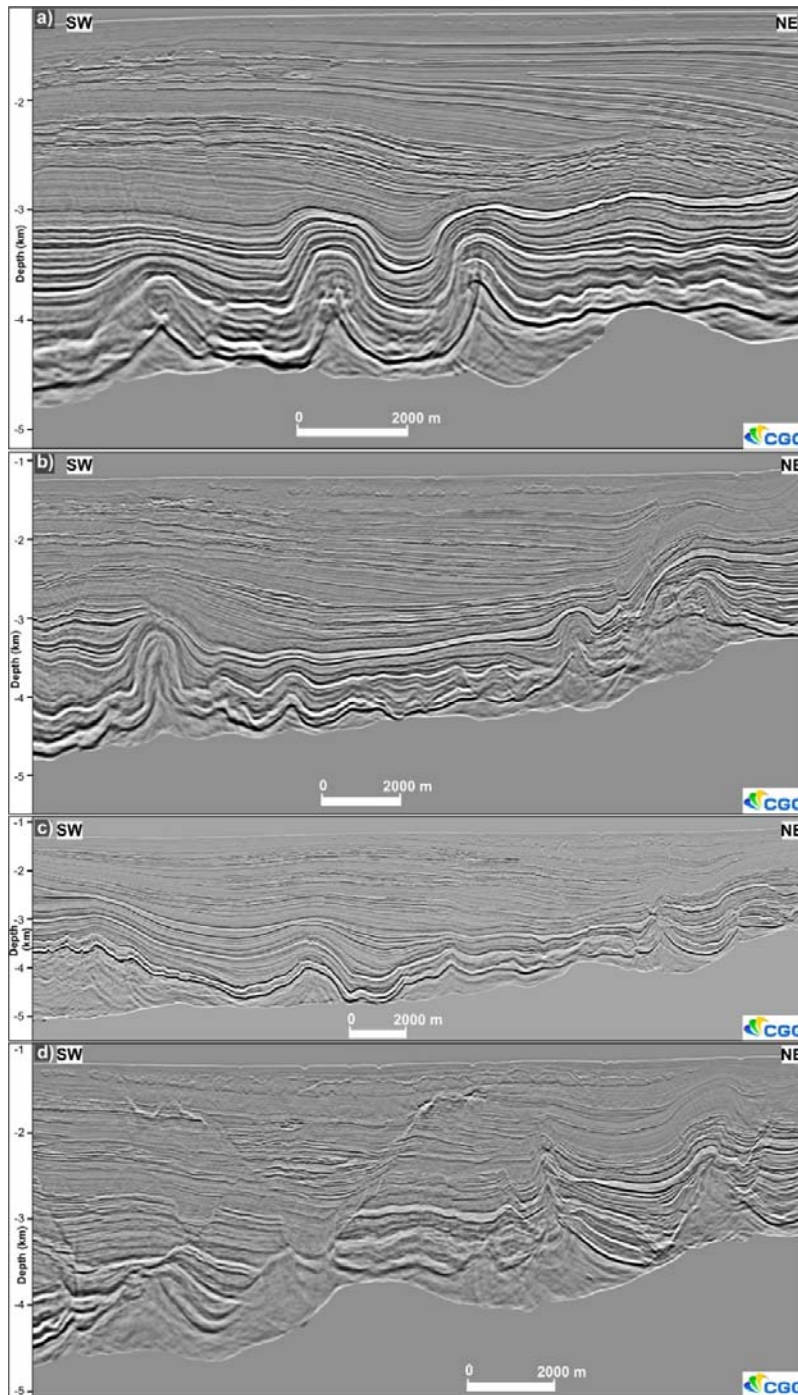
1050

1051
 1052
 1053
 1054

Figure S1. Similar figure with Figure 3 in the main text, illustrating nomenclature and technique to determine geometry of strike-slip faults in this study. (a) oblique view of strike-slip fault; (b) displacement contour on the fault surface; (c) lateral offset and vertical separation displacement profile; (d) hypothetical two-dimensional cross section of a master strike-slip fault; (e) vertical separation-depth; (f) Expansion indices

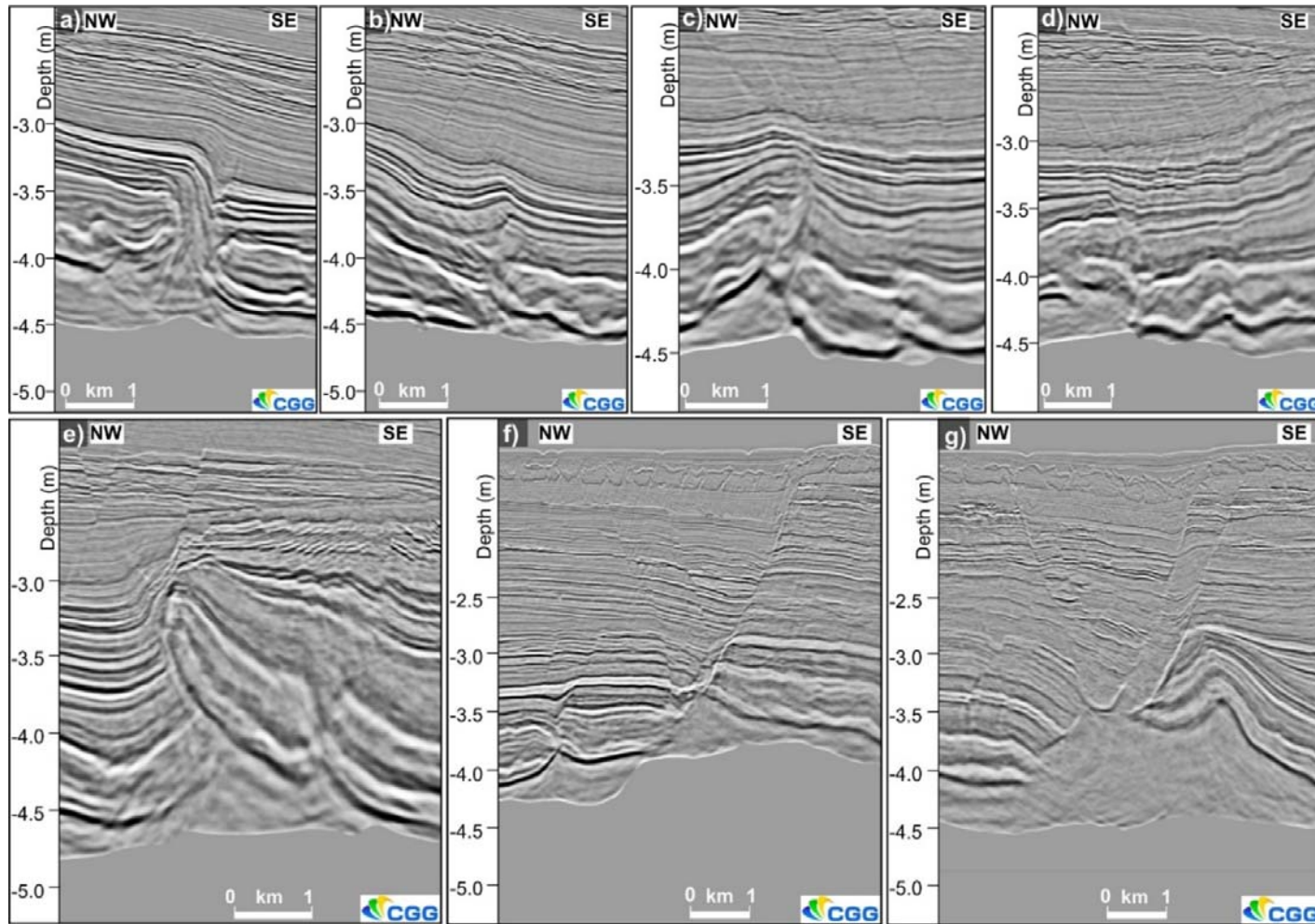
1055 **Appendix B. Uninterpreted seismic cross-section**

1056



1057

1058 Figure S2. Uninterpreted cross section of Figure 9 that are perpendicular to basin margin and across different domains that
1059 are separated by strike-slip faults (section locations shown in Figures 4a-b and 5a in the main text). Seismic data courtesy of
1060 CGG Earth data (previously CGG Multi-Client).

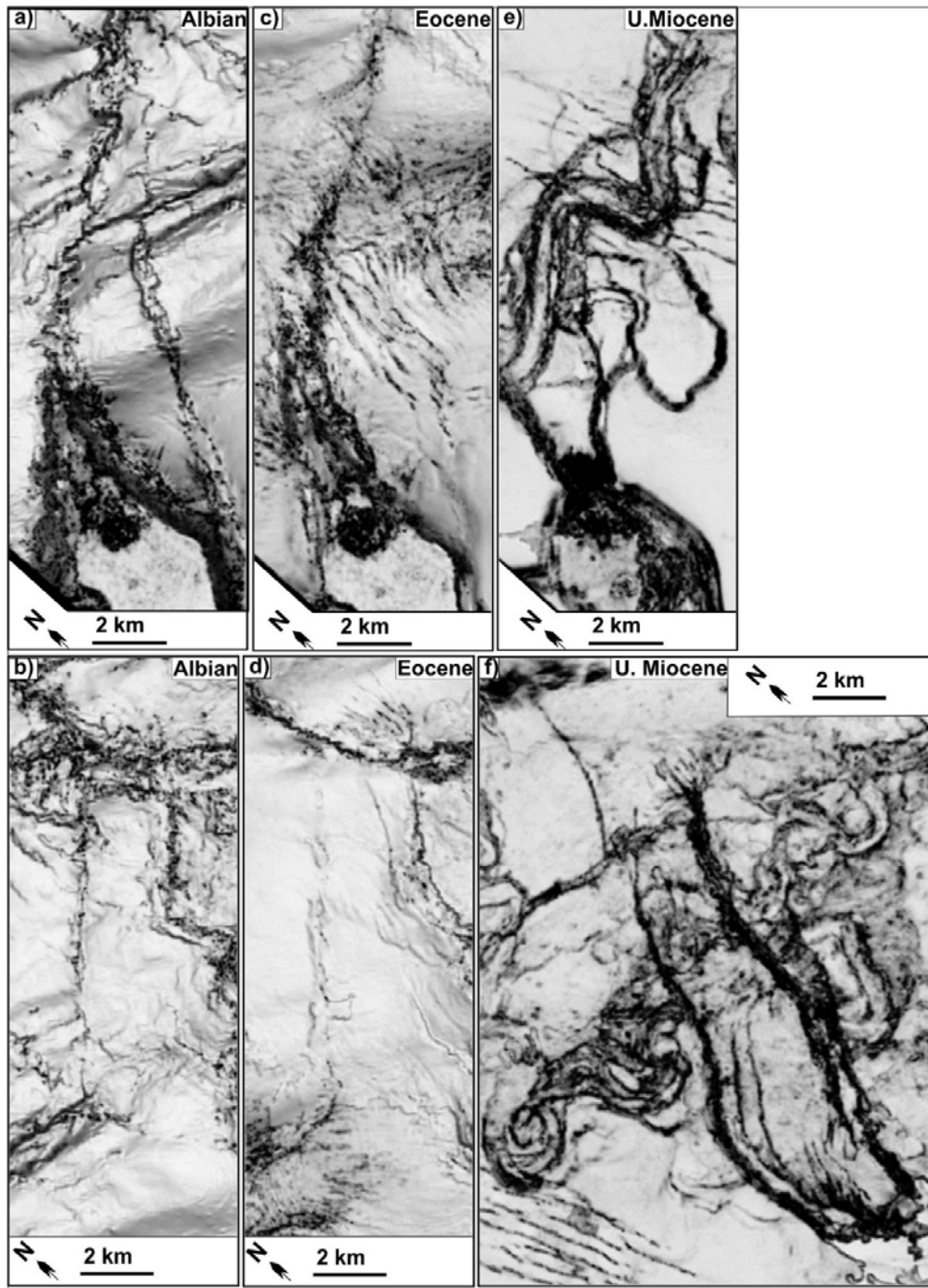


1061

1062
1063

Figure S3. Uninterpreted cross section of Figure 10 across strike-slip faults in the study area (section locations shown in Figures 4a-b and 5a in the main text). Seismic data courtesy of CGG Earth data (previously CGG Multi-Client).

1064 Appendix C. Uninterpreted and interpreted sketch of variance and isopach maps
1065



1066

1067 Figure S4. Uninterpreted zoom in variance map (Figure 6 in main text) at (a-b) Albian, (c-d) Eocene and (e-f) Upper
1068 Miocene structural level, documenting variation of map-view geometry of strike-slip faults (map locations shown in Figure
1069 5). Seismic data courtesy of CGG Earth data (previously CGG Multi-Client).

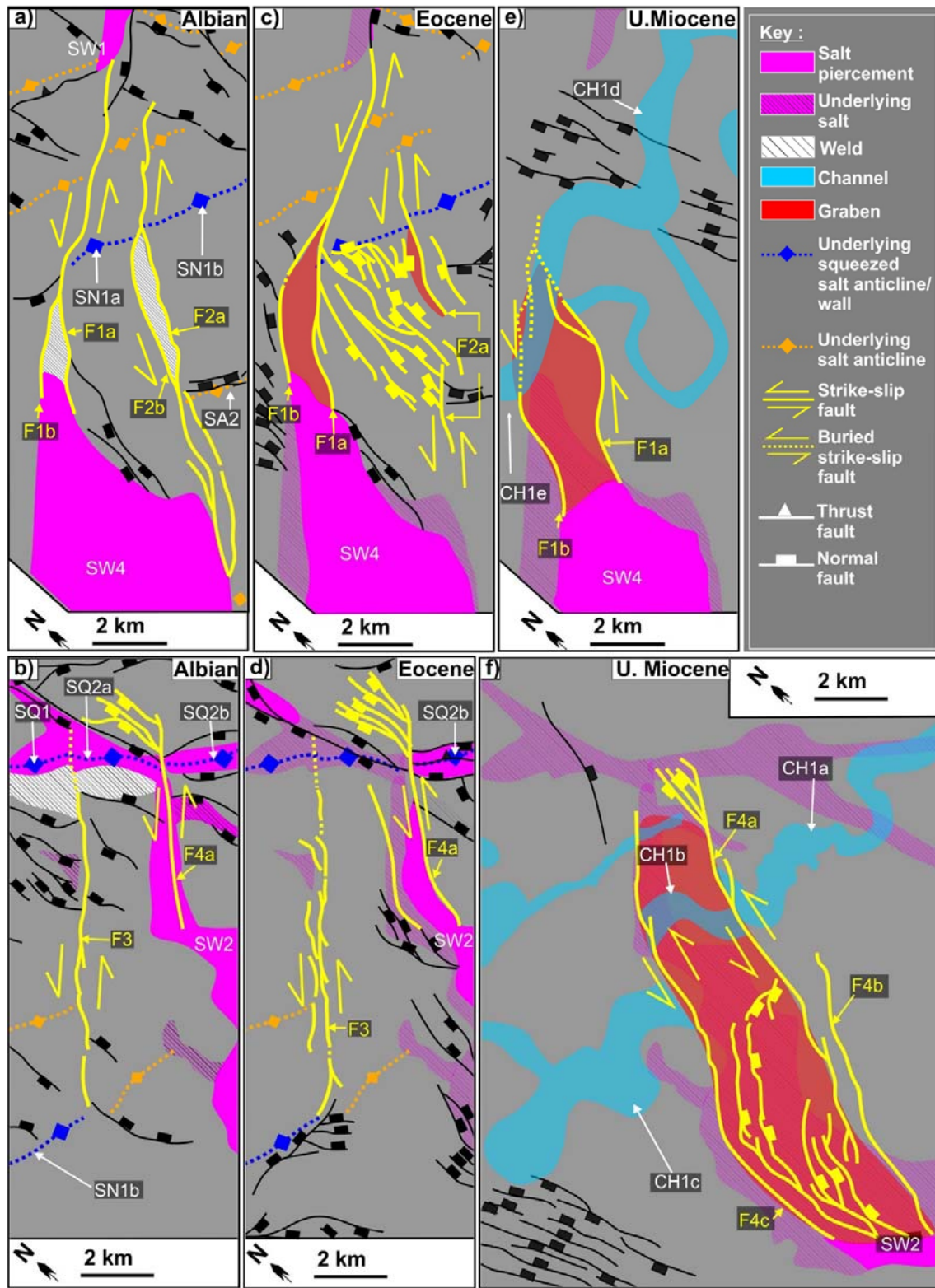
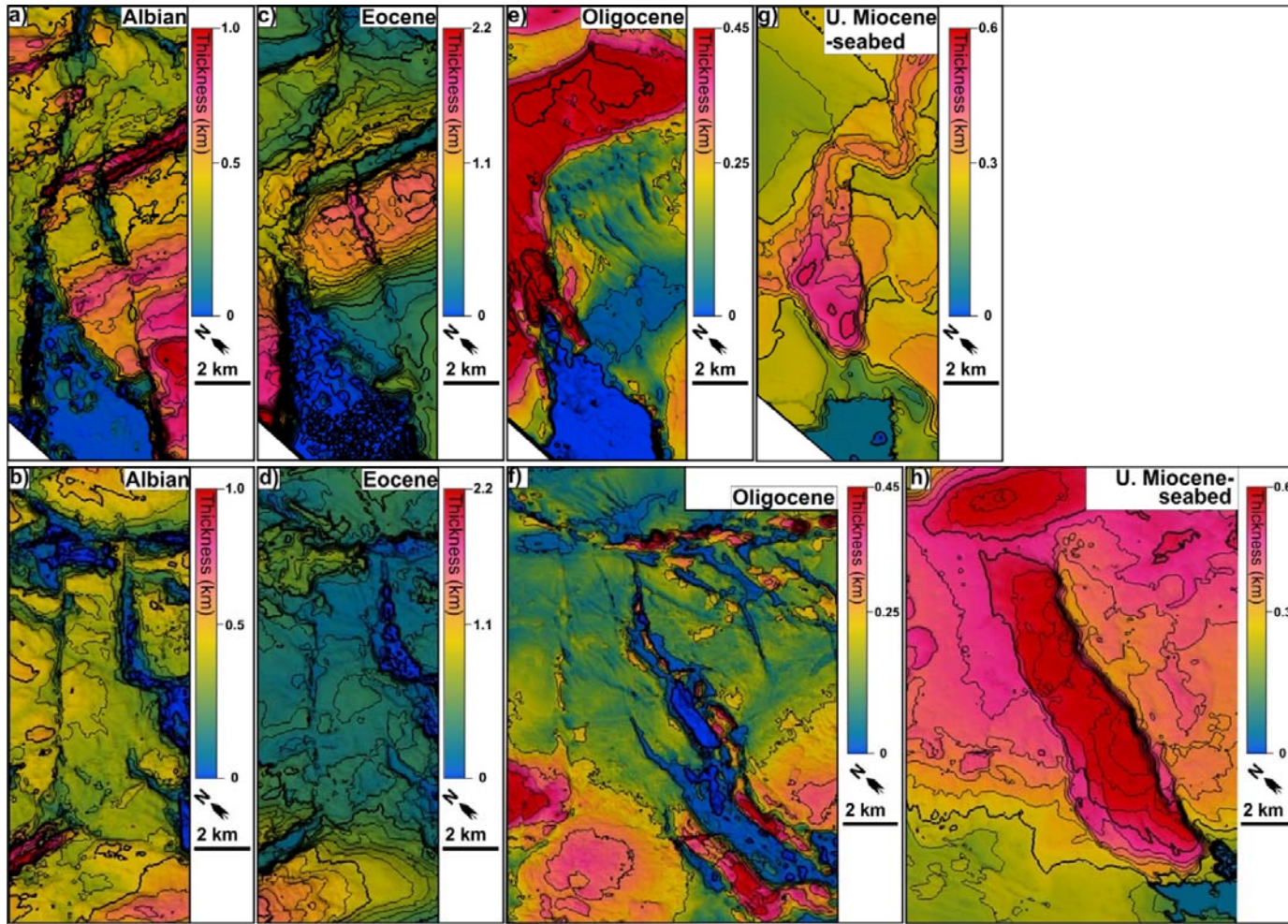
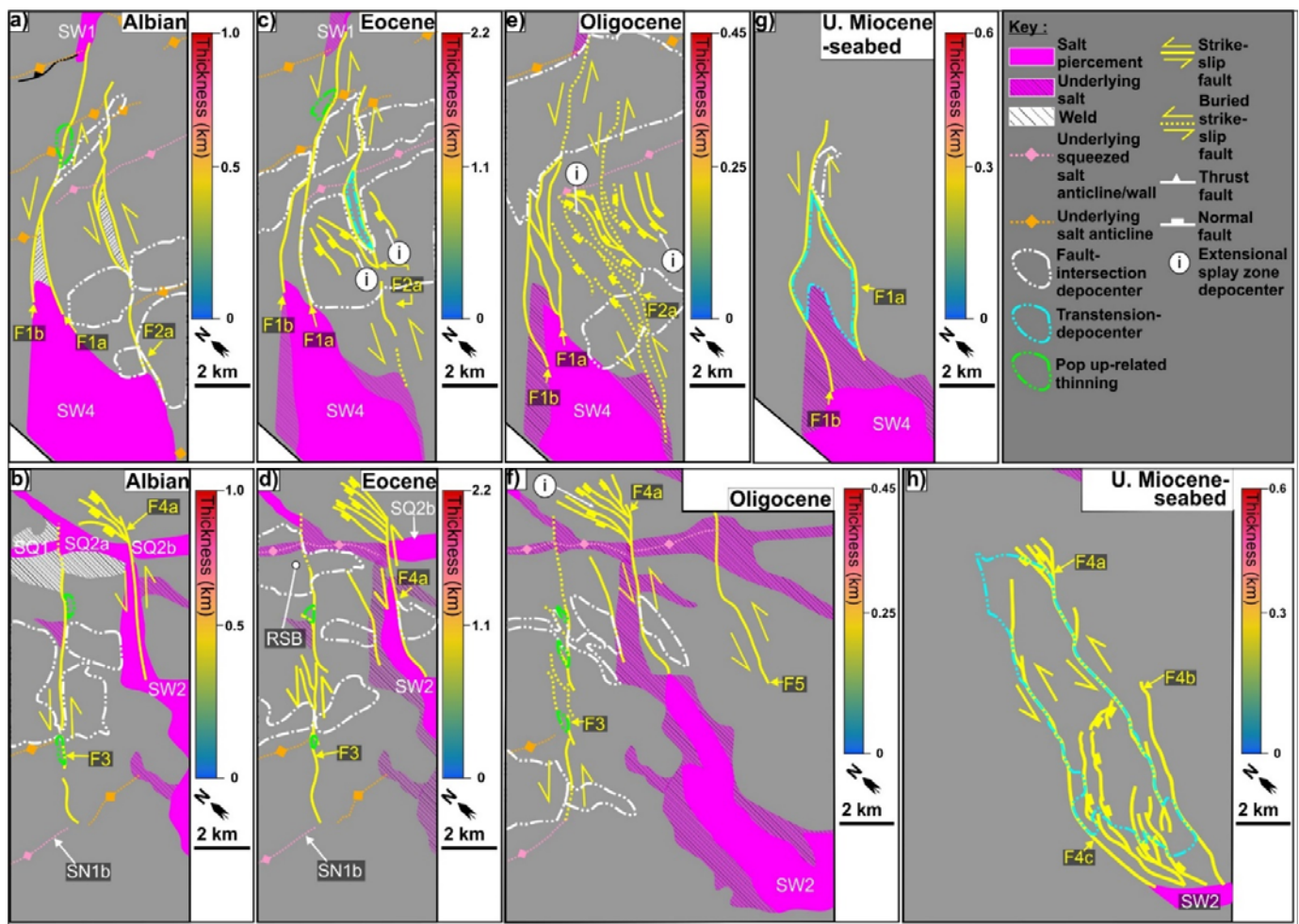


Figure S5. Interpretative sketch map (Figure 6 in main text) of zoom in variance map (Figure S4).



1073

1074 Figure S6. Uninterpreted isopach maps (Figure 7 in main text) of (a-b) Aptian-Albian, (c-d) Albian-Eocene, (e-f) Eocene-Oligocene, (g-h) Upper Miocene to seabed.



1075

1076 Figure S7. Interpretative sketch (Figure 6 in main text) for isopach maps (Figure S6) of (a-b) Aptian-Albian, (c-d) Albian-Eocene, (e-f) Eocene-Oligocene, (g-h) Upper Miocene to seabed.

1077 **Appendix D. Data of salt-detached strike-slip faults and global dataset of strike-slip faults**

1078 **D1. Lateral Offset-distance**

1079 **Table S1.** Dataset for lateral offset-distance in composite displacement-distance and
 1080 thickness variation graph (Figure 8 in main article).

F1a		F2a		F3		F4a&b	
Distance	Offset	Distance	Offset	Distance	Offset	Distance	Offset
0	1683	0	0	0	0	0	0
250	N/A	125	N/A	125	N/A	125	N/A
500		250		250	198	250	
750		375		375	N/A	375	
1000		500		500	384	500	
1250		625		625	N/A	625	
1500		750		750		750	
1750	1441	875		875	241	875	
2000	N/A	1000		1000	N/A	1000	212
2250		1125		1125		1125	
2500		1250	503	1250		1250	
2750		1375		1375		1375	
3000	1379	1500		1500	543	1500	
3250	N/A	1625		1625	N/A	1625	
3500		1750	N/A	1750	915	1750	613
3750	1305	1875		1875	N/A	1875	
4000	N/A	2000		2000		2000	
4250	865	2125		2125		2125	
4500	N/A	2250	336	2250	975	2250	315
4750		2375		2375	N/A	2375	N/A
5000		2500	N/A	2500	890	2500	100
5250		2625		2625	N/A	2625	N/A
5500		2750	429	2750	1027	2750	390
5750	988	2875	N/A	2875	N/A	2875	N/A
6000	1268	3000	450	3000		3000	
6250	N/A	3125	N/A	3125		3125	
6500		3250	324	3250		3250	

6750		3375		3375		3375	
7000		3500	N/A	3500		3500	
7250		3625		3625		3625	
7500	1372	3750	535	3750		3750	
7750	1201	3875		3875		3875	
8000	N/A	4000		4000		4000	434
8250	766	4125		4125		4125	
8500		4250		4250	1038	4250	N/A
8750		4375		4375	N/A	4375	
9000		4500		4500	858	4500	940
9250		4625		4625		4625	N/A
9500		4750		4750	N/A	4750	989
9750		4875	N/A	4875		4875	
10000		5000		5000	545	5000	N/A
10250		5125		5125		5125	
10500	N/A	5250		5250		5250	318
10750		5375		5375		5375	
11000		5500		5500	N/A	5500	N/A
11250		5625		5625		5625	
11500		5750		5750		5750	236
11750		5875		5875		5875	
12000		6000	557	6000	852	6000	N/A
12250		6125		6125		6125	
12500	0	6250		6250		6250	367
12750	N/A	6375		6375		6375	
		6500	N/A	6500	N/A	6500	
		6625		6625		6625	N/A
		6750		6750		6750	
		6875		6875		6875	
		7000	361	7000	327	7000	602
		7125		7125		7125	
		7250	N/A	7250	N/A	7250	N/A
		7375		7375		7375	

	7500	412	7500		7500	
	7625		7625		7625	
	7750		7750		7750	572
	7875		7875		7875	
	8000		8000	879	8000	
	8125		8125		8125	N/A
	8250	N/A	8250		8250	
	8375		8375	N/A	8375	
	8500		8500		8500	593
	8625		8625		8625	
	8750		8750	526	8750	
	8875		8875		8875	
	9000	543	9000		9000	
	9125		9125		9125	
	9250		9250	N/A	9250	
	9375		9375		9375	
	9500		9500		9500	
	9625		9625		9625	
	9750		9750	484	9750	N/A
	9875		9875		9875	
	10000		10000	N/A	10000	
	10125		10125		10125	
	10250		10250	228	10250	
	10375		10375	0	10375	
	10500				10500	
	10625				10625	
	10750				10750	
	10875				10875	
	11000				11000	189
	11125				11125	N/A
	11250				11250	245
	11375				11375	
	11500				11500	N/A

	11625		11625	
	11750	0	11750	200
			11875	N/A
			12000	
			12125	
			12250	
			12375	
			12500	
			12625	
			12750	
			12875	
			13000	
			13125	
			13250	
			13375	
			13500	
			13625	
			13750	
			13875	
			14000	
		14125		
		14250	0	

1082 **D2. Throw-distance (Tx)**

1083 **Table S2.** Dataset for throw-distance in composite displacement-distance and thickness variation graph (Figure 8 in main article).

F1a					F2a				F3				F4a&b								
Distance	Base-salt	Albian	Eocene	Late Miocene	Distance	Base-salt	Albian	Eocene	Distance	Base-salt	Albian	Eocene	Distance	Base-salt	Albian	Eocene	Late Miocene (F4a)	Late Miocene (F4b)			
0	Present	-300	-43	N/A	0	N/A	0	N/A	0	N/A	Albian welding	0	0	N/A	0	0	N/A	N/A			
125		-300	-37		125		-75		125			41	125		-20	-32					
250		-308	-11		250		-60		250			45	250		-40	-40					
375		-370	-12		375		-85		375			45	375		-97	-54					
500		-337	18		500		-92		500			30	500		-82	-45					
625		-272	18		625		-96		625			30	625		-78	-75					
750		-160	89		750		-43		750			-17	750		-85	-103					
875		-183	53		875		0		875			-15	875		-95	-72					
1000		-142	173		1000		-53		1000			-18	1000		-103	-93					
1125		-80	-35		1125		-105		1125			-14	1125		-136	-105					
1250		Albian welding	-41		1250		-173		1250			-10	1250		-150	-211					
1375			-54		1375		-137		1375			-33	1375		-204	-206					
1500			-68		1500		-117		1500			-47	1500		SQ2						
1625			-53		1625		-87		0			1625	Present						-144	-31	1625
1750			-42		1750		-32		-38			1750	-354						-27	1750	

1875		-39	1875	49	-36	1875	-400	-37	1875			
2000	-115	-35	2000	64	-36	2000	-473	-20	2000		0	
2125	-177	-30	2125	53	-62	2125	-525	-16	2125			
2250	-173	0	2250	-65	-106	2250	-458	-20	2250	Albian	-64	-44
2375	-194	10	2375	-40	-88	2375	-325	-40	2375	weldin	-70	-56
2500	-153	20	2500	-113	-94	2500	97	-24	2500	g	-109	-130
2625	-160	38	2625	-184	-65	2625	178	-40	2625		-155	-146
2750	88	60	2750	-294	-53	2750	192	-60	2750		-176	-192
2875	160	74	2875	-362	-49	2875	174	-43	2875	-154	-188	-188
3000	357	85	3000	-500	-83	3000	134	-45	3000	-163	-167	-230
3125	351	70	3125	-378	-86	3125	100	-46	3125	-200	-235	-260
3250	380	72	3250	-247	-109	3250	-61	-70	3250	-247	-238	-272
3375	357	91	3375	-266	-76	3375	-216	-92	3375	-300	-282	-294
3500	363	77	3500	-254	-79	3500	-220	-75	3500	-310	-324	-266
3625	333	76	3625	-287	-66	3625	-237	-31	3625	-341	-343	-263
3750	345	60	3750	-300	-76	3750	-287	-30	3750	-320	-310	-284
3875	330	67	3875	-275	-41	3875	-267	-35	3875	-275	-325	-307
4000	362	63	4000	-366	-20	4000	-89	-26	4000	-281	-325	-309
4125	373	46	4125	-327	-60	4125	-91	-32	4125	-357	-354	-328
4250	373	37	4250	-269	-114	4250	-46	-36	4250	-344	-377	-339
4375	-413	-30	4375	-260	-119	4375	-93	-60	4375	-388	-413	-322
										-409	-421	-345

4500	-465	-27	4500	-257	-103	4500	-89	-84	4500	-379	-437	-310		
4625	-481	-30	4625	-365	-107	4625	-104	-117	4625	-413	-451	-310		
4750	-470	-34	4750	-379	-89	4750	-110	-128	4750	-457	-494	-325		
4875	-444	-37	4875	-355	-78	4875	-117	-120	4875	-451	-514	-351		
5000	-412	-56	5000	-298	-67	5000	-129	-40	5000	-526	-544	-354		
5125	-397	-59	5125	-279	-81	5125	-197	-65	5125	-570	-592	-341		
5250	-346	-57	5250	-260	-57	5250	-186	-100	5250	-538	-586	-355		
5375	-67	-60	5375	-222	-59	5375	-161	-92	5375	-560	-598	-357		
5500	48	94	5500	-200	-23	5500	-116	-111	5500	-561	-598	-368		
5625	88	128	5625	-242	0	5625	-100	-82	5625	-506	-558	-347		
5750	72	146	5750	-296		5750	-105	-51	5750	-530	-510	-338		
5875	171	137	5875	-326		5875	-135	-88	5875	Present	-490	-475	-298	
6000	174	145	6000	-149		6000	-191	-86	6000		-511	-363	-288	
6125	724	136	6125	-177		6125	-202	-72	6125		-552	-329	-274	
6250	786	131	6250	-235		6250	-246	-72	6250		-524	-273	-254	
6375	794	153	6375	Present	N/A	6375	-144	-104	6375		-473	-293	-248	
6500	804	244	6500	-496		6500	-141	-88	6500				-293	
6625	833	233	6625	-515		6625	-161	-87	6625				-301	
6750	800	222	6750	-359		6750	-190	-43	6750		SW2		-306	
6875	767	235	6875	-461		6875	-176	-23	6875				-306	0
7000	709	226	7000	-477		7000	-90	-68	7000				-320	-10

7125	624	239		7125		-385	0	7125		-30	-76	7125		-307	-10
7250	524	289		7250		-183	-50	7250		-24	-76	7250		-310	-10
7375	440	231		7375		-190	-45	7375		34	-53	7375		-307	-10
7500	281	218	0	7500		-269	-42	7500		44	-55	7500		-309	-10
7625	270	192	-13	7625		-273	-52	7625		-26	-50	7625		-312	-12
7750	-197	-143	-26	7750		-279	-49	7750		-72	-52	7750		-324	-22
7875	-235	-139	-28	7875		-240	-46	7875		-105	-43	7875		-357	-30
8000	-250	-128	-25	8000		-204	-43	8000		-108	-46	8000		-359	-40
8125	-229	-146	-46	8125		-178	-38	8125		-121	-57	8125		-375	-35
8250	-214	-181	-47	8250		-172	-33	8250		-144	-36	8250		-381	-43
8375	-198	-231	-51	8375		-164	-24	8375		-147	-60	8375		-387	-51
8500	-172	-231	-56	8500		-165	-15	8500		-99	-47	8500		-373	-62
8625	-180	-268	-70	8625		-152	-19	8625		-54	-31	8625	N/A	-379	-61
8750	-257	-268	-77	8750		-165	-26	8750		-40	-15	8750		-366	-64
8875	-209	-342	-90	8875		-103	-19	8875		0	-37	8875		-350	-72
9000	-198	-434	-78	9000		-66	-17	9000		-90	-53	9000		-336	-78
9125	-203	-513	-92	9125		-59	0	9125		-62	-73	9125		-304	-97
9250	-196	-522	-105	9250	N/A	-66		9250		-63	-55	9250		-307	-102
9375	-140	-679	-120	9375		-114		9375		-95	-62	9375		-303	-112
9500	-157	-680	-124	9500		-107	N/A	9500		-112	-50	9500		-305	-121
9625	-224	-680	-130	9625		-56		9625		-116	-63	9625		-308	-130

9750	-305	-685	-130	9750	-20	9750	-163	-68	9750	-284	-132
9875	-328	-688	-132	9875	-21	9875	-243	-52	9875	-270	-131
10000	N/A	-690	-152	10000	-101	10000	-277	-72	10000	-261	-115
10125		-688	-179	10125	-109	10125	-105	-47	10125	-252	-110
10250		-662	-192	10250	-56	10250	-90	-55	10250	-241	-104
10375		N/A	-199	10375	-40	10375	0	0	10375	-231	-96
10500			-227	10500	-55	10500			10500	-227	-110
10625			-239	10625	-49	10625			10625	-213	-123
10750			-222	10750	-84	10750			10750	-198	-123
10875			-212	10875	-77	10875			10875	-173	-143
11000			-228	11000	-76	11000			11000	-143	-155
11125			-232	11125	-78	11125			11125	-124	-188
11250			-216	11250	-60	11250			11250	-156	-207
11375			-219	11375	-60	11375			11375	-137	-217
11500			-213	11500	-59	11500			11500	-116	-252
11625		-219	11625	-57	11625			11625	-80	-264	
11750		-183	11750	0	11750			11750	-52	-276	
11875		-153			11875			11875	-30	-302	
12000		-132			12000			12000	-13	-340	
12125	-121			12125			12125	-10	-333		
12250	-127			12250			12250	-10	-362		

12375			-76		12375		0	-375
12500			-22		12500			-376
12625			-16		12625			-385
12750			0		12750			-392
					12875			-387
					13000			-382
					13125		N/A	-367
					13250			-350
					13375			-331
					13500			-327
					13625			-224
					13750			-70

1085 **D3 Global and our dataset of strike-slip faults**

1086 **Table S3.** Global and our dataset containing of maximum displacement against fault length for
 1087 strike-slip faults (Figure 14e in main article).

Reference	Length (Log 10 ^s)	Maximum displacement (Log 10 ^s)
Mc Millan (1975)	4.583	2.999
	4.924	3.304
	5.350	3.560
	5.229	3.685
	5.117	3.761
	5.202	3.968
	5.354	3.959
	5.619	3.963
	5.471	4.102
	5.570	4.133
	5.354	4.156
	5.256	4.160
	5.139	4.151
	4.973	4.089
	4.937	3.976
	4.933	3.869
	4.848	3.770
	4.597	3.667
	4.552	3.757
	4.641	3.878
4.543	3.873	
4.588	3.976	
4.498	3.972	

4.493	4.039
4.606	4.142
4.709	4.142
4.713	3.976
4.830	4.138
4.749	4.151
4.830	4.295
4.915	4.142
4.933	4.286
4.834	4.434
4.942	4.447
5.036	4.295
5.130	4.281
5.224	4.286
5.287	4.286
5.399	4.286
5.547	4.277
5.659	4.277
5.502	4.366
5.493	4.420
5.556	4.505
5.650	4.465
5.722	4.425
5.937	4.456
6.126	4.389
5.860	4.592
5.421	4.611
5.356	4.443
5.253	4.513
5.155	4.457
5.183	4.373

	4.963	4.485
	4.949	4.583
	4.935	4.681
	4.828	4.695
	4.921	4.713
	5.141	4.816
	5.141	4.690
	5.127	4.863
	5.244	4.961
	5.342	4.793
	5.426	4.816
	5.328	5.003
	5.468	4.923
	5.561	4.905
	5.543	4.993
	5.645	4.695
	5.720	4.891
	5.711	5.073
	5.706	5.143
	5.725	5.269
	5.870	5.264
	5.874	5.367
	5.785	5.479
	5.683	5.381
	5.622	5.381
	5.930	5.572
	6.010	5.171
	6.010	5.073
	5.949	5.003
Wesnousky (1988)	1.861	1.543

Peacock (1991)	-0.636	-1.733
	-0.030	-1.684
	-0.292	-1.275
	-0.095	-1.144
Kim et al (2000; Isolated Faults)	0.561	-1.832
	0.523	-1.976
	0.166	-2.020
	0.054	-2.089
	-0.172	-2.295
	0.091	-2.308
	0.173	-2.295
	-0.147	-2.395
	-0.397	-2.370
	-0.435	-2.539
	-0.685	-2.696
0.348	-2.696	
0.199	-2.170	
Kim et al (2000; Interacting fault)	0.081	-0.871
	0.125	-1.172
	-0.100	-1.370
	0.054	-0.723
	0.350	-0.652
	0.718	-0.476
	0.778	-0.570
	0.986	-0.465
	1.074	-0.317
	0.833	-0.718
	0.761	-0.800
	0.586	-0.893
	0.888	-0.811
0.761	-1.096	

	0.454	-1.090
	0.564	-1.107
	0.361	-1.211
	0.389	-1.310
	0.240	-1.468
	0.487	-1.479
	1.442	-0.663
	1.425	-0.531
	1.568	-0.690
	1.647	0.485
	2.035	0.659
Sieh and Natawidjaja (2000)	2.044	1.356
Walker and Jackson (2002)	1.448	1.074
Jachens et al. (2002)	1.001	0.474
	0.908	0.844
Tatar et al. (2004)	1.566	0.996
	1.418	1.657
Rovida and Tibaldi (2005)	-0.727	0.224
Fu and Awata (2006)	2.528	1.995
Nemer and Meghraoui (2006)	0.830	0.926
de Joussineau and Ayidin (2009)	-0.923	-1.923
	-1.110	-1.854
	-0.699	-1.102
	-0.550	-1.068

	-1.007	-0.761
	-0.484	-0.224
	-0.176	0.378
F1a (Our study)	3.641	3.140
	3.923	3.137
F2a (Our study)	3.352	2.702
	3.699	2.728
	3.653	2.735
F3 (Our study)	3.699	3.016
	3.352	2.930
	3.495	2.944
F4a&b (Our study)	3.439	2.787
	3.528	2.995
	3.875	2.780

1089 **References**

- 1090 Cartwright, J. A., & Mansfield, C. S. (1998). Lateral displacement variation and lateral tip
1091 geometry of normal faults in the Canyonlands National Park, Utah. *Journal of Structural*
1092 *Geology*, 20(1), 3-19. doi:10.1016/s0191-8141(97)00079-5
- 1093 Chapman, T. J., & Meneilly, A. W. (1991). The displacement patterns associated with a reverse-
1094 reactivated, normal growth fault. *Geological Society, London, Special Publications*, 56(1), 183-
1095 191. doi:10.1144/gsl.sp.1991.056.01.12
- 1096 de Joussineau, G., & Aydin, A. (2009). Segmentation along Strike-Slip Faults Revisited. 1575-
1097 1594. doi:10.1007/978-3-0346-0138-2_3
- 1098 Deng, S., Li, H., Zhang, Z., Zhang, J., & Yang, X. (2019). Structural characterization of
1099 intracratonic strike-slip faults in the central Tarim Basin. *AAPG Bulletin*, 103(1), 109-137.
1100 doi:10.1306/06071817354
- 1101 Dutton, D. M., & Trudgill, B. D. (2009). Four-dimensional analysis of the Sembo relay system,
1102 offshore Angola: Implications for fault growth in salt-detached settings. *AAPG Bulletin*, 93(6),
1103 763-794. doi:10.1306/02230908094
- 1104 Fu, B., & Awata, Y. (2007). Displacement and timing of left-lateral faulting in the Kunlun Fault
1105 Zone, northern Tibet, inferred from geologic and geomorphic features. *Journal of Asian Earth*
1106 *Sciences*, 29(2), 253-265. doi:<https://doi.org/10.1016/j.jseaes.2006.03.004>
- 1107 Jachens, R. C., Langenheim, V. E., & Matti, J. C. (2002). Relationship of the 1999 Hector Mine
1108 and 1992 Landers Fault Ruptures to Offsets on Neogene Faults and Distribution of Late
1109 Cenozoic Basins in the Eastern California Shear Zone. *Bulletin of the Seismological Society of*
1110 *America*, 92(4), 1592-1605. doi:10.1785/0120000915
- 1111 Jackson, C. A. L., Bell, R. E., Rotevatn, A., & Tvedt, A. B. M. (2017). Techniques to determine
1112 the kinematics of synsedimentary normal faults and implications for fault growth models.
1113 *Geological Society, London, Special Publications*, 439(1), 187-217. doi:10.1144/sp439.22
- 1114 Jackson, C. A. L., & Rotevatn, A. (2013). 3D seismic analysis of the structure and evolution of a
1115 salt-influenced normal fault zone: A test of competing fault growth models. *Journal of Structural*
1116 *Geology*, 54, 215-234. doi:10.1016/j.jsg.2013.06.012

- 1117 Kim, Y.-S., Andrews, J. R., & Sanderson, D. J. (2000). Damage zones around strike-slip fault
1118 systems and strike-slip fault evolution, Crackington Haven, southwest England. *Geosciences*
1119 *Journal*, 4(2), 53. doi:10.1007/BF02910127
- 1120 Kim, Y.-S., Andrews, J. R., & Sanderson, D. J. (2001). Reactivated strike-slip faults: examples
1121 from north Cornwall, UK. *Tectonophysics*, 340(3-4), 173-194. doi:10.1016/s0040-
1122 1951(01)00146-9
- 1123 Kim, Y.-S., & Sanderson, D. J. (2005). The relationship between displacement and length of
1124 faults: a review. *Earth-Science Reviews*, 68(3-4), 317-334. doi:10.1016/j.earscirev.2004.06.003
- 1125 Mansfield, C. S., & Cartwright, J. (1996). High resolution fault displacement mapping from
1126 three-dimensional seismic data: evidence for dip linkage during fault growth.
- 1127 McMillan, R. A. (1975). *The orientation and sense of displacement of strike-slip faults in*
1128 *continental crust*. (Bachelor). Carleton University, Ottawa, Ontario.
- 1129 Nemer, T., & Meghraoui, M. (2006). Evidence of coseismic ruptures along the Roum fault
1130 (Lebanon): a possible source for the AD 1837 earthquake. *Journal of Structural Geology*, 28(8),
1131 1483-1495. doi:<https://doi.org/10.1016/j.jsg.2006.03.038>
- 1132 Nixon, C. W., Sanderson, D. J., & Bull, J. M. (2011). Deformation within a strike-slip fault
1133 network at Westward Ho!, Devon U.K.: Domino vs conjugate faulting. *Journal of Structural*
1134 *Geology*, 33(5), 833-843. doi:10.1016/j.jsg.2011.03.009
- 1135 Omosanya, K. O., Zervas, I., Mattos, N. H., Alves, T. M., Johansen, S. E., & Marfo, G. (2017).
1136 Strike-Slip Tectonics in the SW Barents Sea During North Atlantic Rifting (Swaen Graben,
1137 Northern Norway). *Tectonics*, 36(11), 2422-2446. doi:10.1002/2017TC004635
- 1138 Pan, S., Bell, R. E., Jackson, C. A. L., & Naliboff, J. (2022). Evolution of normal fault
1139 displacement and length as continental lithosphere stretches. *Basin Research*, 34(1), 121-140.
1140 doi:<https://doi.org/10.1111/bre.12613>
- 1141 Peacock, D. C. P. (1991). Displacements and segment linkage in strike-slip fault zones. *Journal*
1142 *of Structural Geology*, 13(9), 1025-1035. doi:10.1016/0191-8141(91)90054-m
- 1143 Petersen, K., Clausen, O. R., & Korstgård, J. A. (1992). Evolution of a salt-related listric growth
1144 fault near the d-1 well, block 5605, danish north sea: displacement history and salt kinematics.

1145 *Journal of Structural Geology*, 14(5), 565-577. doi:[https://doi.org/10.1016/0191-8141\(92\)90157-](https://doi.org/10.1016/0191-8141(92)90157-)
1146 [R](#)

1147 Reeve, M. T., Bell, R. E., Duffy, O. B., Jackson, C. A. L., & Sansom, E. (2015). The growth of
1148 non-colinear normal fault systems; What can we learn from 3D seismic reflection data? *Journal*
1149 *of Structural Geology*, 70, 141-155. doi:10.1016/j.jsg.2014.11.007

1150 Rovida, A., & Tibaldi, A. (2005). Propagation of strike-slip faults across Holocene volcano-
1151 sedimentary deposits, Pasto, Colombia. *Journal of Structural Geology*, 27(10), 1838-1855.
1152 doi:<https://doi.org/10.1016/j.jsg.2005.06.009>

1153 Rowan, M. G., Hart, B. S., Nelson, S., Flemings, P. B., & Trudgill, B. D. (1998). Three-
1154 dimensional geometry and evolution of a salt-related growth-fault array: Eugene Island 330 field,
1155 offshore Louisiana, Gulf of Mexico. *Marine and Petroleum Geology*, 15(4), 309-328.
1156 doi:10.1016/s0264-8172(98)00021-x

1157 Sieh, K., & Natawidjaja, D. (2000). Neotectonics of the Sumatran fault, Indonesia. *Journal of*
1158 *Geophysical Research: Solid Earth*, 105(B12), 28295-28326.
1159 doi:<https://doi.org/10.1029/2000JB900120>

1160 Tatar, O., Piper, J. D. A., Gürsoy, H., Heimann, A., & Koçbulut, F. (2004). Neotectonic
1161 deformation in the transition zone between the Dead Sea Transform and the East Anatolian Fault
1162 Zone, Southern Turkey: a palaeomagnetic study of the Karasu Rift Volcanism. *Tectonophysics*,
1163 385(1), 17-43. doi:<https://doi.org/10.1016/j.tecto.2004.04.005>

1164 Thorsen, C. E. (1963). Age of growth faulting in south-east Louisiana. *Gulf Coasts Association of*
1165 *Geologists Societies Transactions*, 13, 103-110.

1166 Tvedt, A. B. M., Rotevatn, A., & Jackson, C. A. L. (2016). Supra-salt normal fault growth during
1167 the rise and fall of a diapir: Perspectives from 3D seismic reflection data, Norwegian North Sea.
1168 *Journal of Structural Geology*, 91, 1-26. doi:10.1016/j.jsg.2016.08.001

1169 Walker, R., & Jackson, J. (2002). Offset and evolution of the Gowk fault, S.E. Iran: a major
1170 intra-continental strike-slip system. *Journal of Structural Geology*, 24(11), 1677-1698.
1171 doi:[https://doi.org/10.1016/S0191-8141\(01\)00170-5](https://doi.org/10.1016/S0191-8141(01)00170-5)

1172 Walsh, J. J., & Watterson, J. (1988). Analysis of the relationship between displacements and
1173 dimensions of faults.

1174 Wesnousky, S. G. (1988). Seismological and structural evolution of strike-slip faults. *Nature*,
1175 335(6188), 340-343. doi:10.1038/335340a0

1176